THESIS FOR THE DEGREE OF LICENTIATE OF ENGINEERING

Tyre aerodynamics of passenger vehicles

ERIK JOSEFSSON

Department of Mechanics and Maritime Sciences

CHALMERS UNIVERSITY OF TECHNOLOGY

Gothenburg, Sweden 2022

Tyre aerodynamics of passenger vehicles
ERIK JOSEFSSON

Thesis for the degree of Licentiate of Engineering 2022:02
Department of Mechanics and Maritime Sciences
Chalmers University of Technology
SE-412 96 Gothenburg
Sweden
Telephone: +46 (0)31-772 1000

Chalmers Digitaltryck
Gothenburg, Sweden 2022

Tyre aerodynamics of passenger vehicles
ERIK JOSEFSSON
Department of Mechanics and Maritime Sciences
Chalmers University of Technology

Abstract

To decelerate climate change and limit global warming, there is a need for reducing the environmental impact of vehicles, which can be achieved by increasing their energy efficiency. For a passenger vehicle, one of the largest resistive forces is aerodynamic drag. A significant contribution to the total drag originates from the wheels, making the understanding of their flows essential for creating efficient vehicles. However, wheel flows are complex and challenging to comprehend due to factors such as the rotation, high level of geometrical details and tyre deformation, all of which have been shown to affect drag. For a better understanding, numerical simulations can be used. However, to determine the accuracy of the simulations, these must be correlated to experiments.

In this work, both the correlation between experiments and simulations as well as the flow field effect of varying the tyre tread pattern are investigated. Wind tunnel tests using a full-scale DrivAer model have been performed for four tyre tread patterns and two rim designs. First, the numerical simulations are compared to the experiments, where the interference of the wind tunnel on wheel flows is investigated. By performing simulations using both an open road domain and a domain containing a detailed model of the wind tunnel, it was found that the inclusion of the wind tunnel improves predictions of both absolute drag values as well as the drag deltas between configurations.

Then, the effects of the different tyre tread patterns are analysed in more detail. Results showed that adding rain grooves typically reduces drag compared to a slick tyre, whereas the effect of lateral grooves is dependent on the rim configuration. In addition to the drag, lift variations were considered. There, the largest effects were obtained at the front axle and, in general, the lift is reduced by the rain grooves and increased by the lateral grooves, most clearly for the closed rim. Also, the influence of the parasitic lift forces acting on the wheel drive units was demonstrated.

Keywords: aerodynamics, wheels, tyres, drag, wind tunnel, CFD

Acknowledgements

First of all, I would like to thank my main supervisor, Prof. Simone Sebben, for all her support and guidance, helping me develop. Much of this work would not have been possible without the support of the people at Volvo Cars. In particular, I would like to thank Dr. Teddy Hobeika for sharing his expertise on tyre aerodynamics and always being supportive. Additionally, thank you to Alexander Broniewicz and Dr. Magnus Urquhart for their contributions in the early and recent stages of this project, respectively.

This project is financed by the Swedish Energy Agency and Volvo Cars. The simulations were performed on the computational cluster of Volvo Cars and resources provided by the Swedish National Infrastructure for Computing (SNIC).

The work presented in this thesis is based on experiments with the DrivAer geometry which was kindly provided by Ford of Europe. Particularly, I would like to acknowledge Dr. Burkhard Hupertz and Manfred Lentzen for enabling the collaboration and sharing their expertise on the model.

I would like to express my gratitude towards my colleagues and friends at VEAS. Thank you for all the fun activities and enlightening discussions. You create an excellent and inspiring work environment. A special thanks to Sonja for bringing the division together and always being helpful.

Finally, I would like to thank my family for all the support you have given me, encouraging me to pursue my goals. To Frida, thank you for all the love, care and for distracting me from work when I need it the most.

Erik Josefsson
Gothenburg, March 2022

Nomenclature

Abbreviations

CAE	Computer Aided Engineering
CFD	Computational Fluid Dynamics
CFL	Courant–Friedrichs–Lewy
EU	European Union
Exp	Experimental
FW	Front Wheel
IDDES	Improved Delayed Detached Eddy Simulation
LES	Large Eddy Simulation
MRF	Moving Reference Frame
MRFg	Moving Reference Frame - grooves
PVT	Volvo Cars Aerodynamic Wind Tunnel
RW	Rear Wheel
SM	Sliding Mesh
SST	Shear Stress Transport
URANS	Unsteady Reynolds Averaged Navier-Stokes
WDU	Wheel Drive Unit
WLTP	Worldwide harmonized Light vehicles Test Procedure

Configurations

CR	Closed Rim
D	Detailed tyre
L	Lateral grooved tyre
OR	Open Rim
R	Rain grooved tyre
S	Slick tyre

Symbols

α	Road inclination angle	[°]
ΔP	Pressure drop over wind tunnel contraction	[Pa]
ω_i	Vorticity component in i-direction	[1/s]
$\overline{\xi}$	Mean component of ξ	[ξ]
ρ	Air density	[kg/m^3]
$\vec{x}$	Spatial vector	[m]
ξ'	Fluctuating component of ξ	[ξ]

ξ'_{RMS}	Root mean square value of ξ	$[\xi]$
ξ_∞	Freestream value of ξ	$[\xi]$
A	Vehicle frontal area	$[\mathrm{m}^2]$
C_ξ^{norm}	Normalised two-point correlation of ξ	$[-]$
C_D	Drag coefficient	$[-]$
C_L	Lift coefficient	$[-]$
C_p	Pressure coefficient	$[-]$
C_{LF}	Front lift coefficient	$[-]$
C_{LR}	Rear lift coefficient	$[-]$
C_{ptot}	Total pressure coefficient	$[-]$
F_R	Resistive force	[N]
f_r	Rolling resistance coefficient	$[-]$
k_p	Calibration coefficient for wind tunnel static pressure	$[-]$
k_q	Calibration coefficient for wind tunnel dynamic pressure	$[-]$
m	Vehicle mass	[kg]
P	Static pressure	[Pa]
P_∞	Reference pressure	[Pa]
P_{C1}	Pressure upstream wind tunnel contraction	[Pa]
P_{C2}	Pressure downstream wind tunnel contraction	[Pa]
t	Time	[s]
U_∞	Reference velocity	[m/s]
v	Velocity magnitude	[m/s]
v_i	Velocity component in i-direction	[m/s]

Thesis

This thesis consists of an extended summary of the following appended papers:

Paper A Josefsson, E., Hobeika, T., and Sebben, S. "Evaluation of Wind Tunnel Interference on Numerical Prediction of Wheel Aerodynamics". *Accepted for publication in Journal of Wind Engineering and Industrial Aerodynamics* (2022)

Paper B Josefsson, E., Hobeika, T., Sebben, S., and Urquhart, M. "Investigation of Tyre Pattern Effect on the Aerodynamics of a Passenger Vehicle". *Submitted to Journal of Fluids Engineering* (2022)

Division of work

The wind tunnel test was planned by Josefsson with input from all authors and representatives from Ford of Europe. The testing was performed by Josefsson and Hobeika, with assistance from a Ford representative. All simulations were set up, performed and analysed by Josefsson based on scripts provided by Volvo Cars, which were modified by Josefsson during the method development. The results were analysed by Josefsson, who also wrote the original manuscripts. The results and manuscripts were discussed and reviewed by the co-authors.

Contents

Part I

Extended summary

1

Introduction

Transportation is a central part of today's society, enabling the movement of people and goods. In particular, passenger vehicles are an important part of transportation, allowing people to move freely. However, passenger vehicles are also responsible for significant greenhouse gas emissions. For example, in 2019, they were responsible for 12% of the emissions in the EU [3]. Hence, there is a need for improving their energy efficiency. This need is reflected in legislation, where stricter emission limits are being employed [4] along with a new method for certifying vehicles, the Worldwide harmonized Light vehicles Test Procedure (WLTP) [5].

The energy efficiency of vehicles can be improved by reducing the aerodynamic drag. For a passenger vehicle, a significant part of the drag originates from the wheels, making them an important aspect of the total aerodynamic performance. Because of the rotation and bluff-body geometry of the wheels, the flow field is complex and challenging to comprehend. Furthermore, significant differences in the flow can occur even from small geometrical changes of tyre features such as the profile, deformation or tread pattern. Due to the complexity and sensitivity of the flow, there is a need for a better understanding of which aspects affect the aerodynamic performance of tyres.

To improve this understanding, numerical simulations can be used, allowing detailed investigations of the flow field, even in places where physical measurements are constrained. Moreover, the WLTP regulations require that emission levels are specified for all vehicle configurations, creating a need for accurate and efficient numerical methods able to predict changes between wheel configurations. To establish the accuracy of the simulations, these must be correlated to wind tunnel experiments. However, simulations are typically performed in conditions replicating open road, where the blockage is negligible and the ground plane is fully moving, varying from those of wind tunnels. In order to correlate CFD and experiments, the differences between the two environments, and how they impact the results, must be understood.

This thesis investigates how variations in the tread pattern affect the aerodynamics of a passenger vehicle. Full-scale wind tunnel tests, capturing forces, surface pressures and flow fields, were performed using the DrivAer reference geometry combined with four tread patterns and two rim designs. The experimental results are compared to numerical simulations replicating both open road and wind tunnel conditions. Initially, the effect of including the wind tunnel geometry and its moving ground system in the simulation is considered in terms of the ability to predict wheel flows. Next, the flow fields created by the various tread patterns are presented and the impacts on the aerodynamic forces are analysed.

1.1 Research objectives

This thesis is part of a PhD project at Chalmers University of Technology in collaboration with Volvo Cars. The main objective of the project is to improve the knowledge of tyre aerodynamics and how it affects the total aerodynamic performance of vehicles. This objective will be achieved by considering the following sub-objectives:

- Identify which features influence the flow around tyres and how they affect drag and lift.
- Determine a suitable level of complexity for reliable and effective numerical simulations.
- Develop wind tunnel corrections for lift force measurements.
- Develop methods for measuring tyre deformation due to static loads and rotation.

As this thesis is part of an ongoing PhD project, it does not cover all aspects of the objectives. Here, the first objective will be investigated for varying tread patterns, with a brief connection to the third objective when considering the lift forces. The second objective is investigated in terms of the need for including the wind tunnel geometry in simulations. For the fourth objective, a method for replicating the static deformation is presented.

1.2 Limitations

- The project is limited in terms of experimental and numerical resources, restricting the number of configurations that could be investigated.
- Only one vehicle, the DrivAer, and one baseline tyre geometry, for which the tread pattern was varied, was considered.
- Given the limitation of wind tunnel time and the available measurement equipment, only selected regions of the flow were investigated with flow field measurements.

1.3 Outline

Chapter 1 presented the context of tyre aerodynamics along with the objectives and limitations of the project. In Chapter 2, the relevant background is presented. The connection between environmental impact and vehicle aerodynamics is discussed along with a review of previous research. Chapter 3 presents the experimental and numerical setups of the investigation. Next, the results are split into two parts with Chapter 4 focusing on wind tunnel interference and its impact on wheel aerodynamics and Chapter 5 covering the impact of various tread patterns. Finally, some concluding remarks and future work are presented in Chapter 6 along with a summary of the appended papers, Chapter 7.

2

Background

This chapter introduces the background relevant to the project. Firstly, the motivation behind this thesis is presented in terms of environmental impact and the role of the passenger vehicle. Next, a review of previous research on tyre aerodynamics is given.

2.1 Environmental aspects

Greenhouse gas emissions contribute to global warming and climate change. Within the EU, 29% of the emissions originate from the transport sector [3]. Within this share, the majority is generated by road transport, with 43% coming from passenger vehicles, Figure 2.1. Hence, improving the efficiency of passenger cars is important for reducing environmental impact.

The resistive force, F_R, acting on a vehicle while driving can be split into the following components

$$F_R = m\frac{dv}{dt} + mg\sin\alpha + f_r mg\cos\alpha + \frac{C_D A\rho v^2}{2}, \tag{2.1}$$

where the first term represents the force required for accelerating, the second describes the force needed for overcoming a road gradient α, the third is rolling resistance and the fourth is the aerodynamic drag. Assuming constant velocity and no road inclination Equation (2.1)

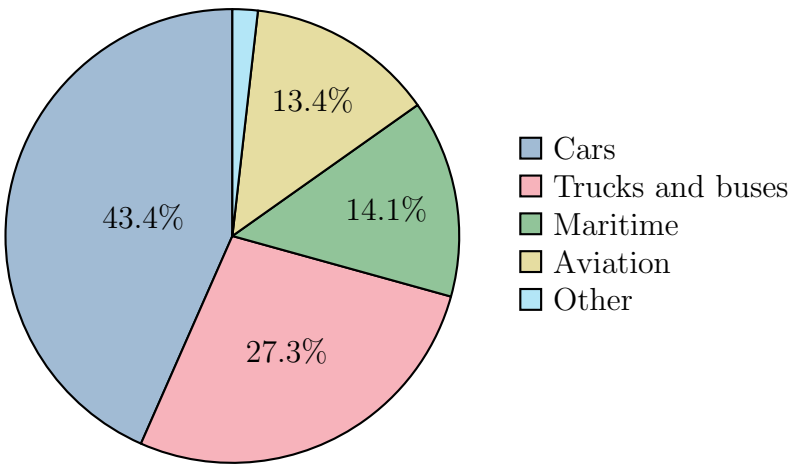

Figure 2.1: *Distribution of greenhouse gas emissions within the transport sector during 2019. From the European Environment Agency [3].*

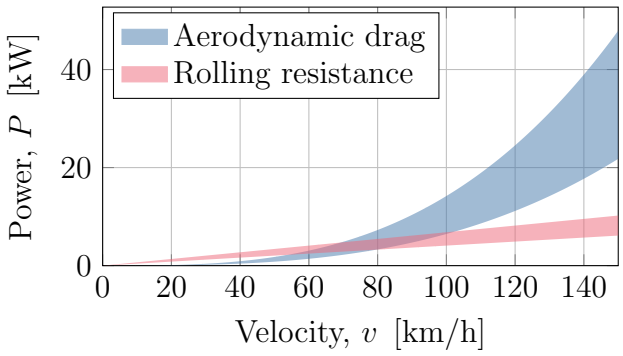

Figure 2.2: *Power required to overcome drag and rolling resistance. The mass and C_DA are assumed to be in the range* 1500 *to* 2500 kg *and* 0.5 *to* 1.1 m^2*, respectively. The rolling resistance is taken as* $f_r = 0.010$*. [6]*

simplifies to only rolling resistance and drag. Given F_R, the power needed to propel the vehicle can be calculated as

$$P = vF_R = vf_rmg\cos\alpha + \frac{C_DA\rho v^3}{2}. \tag{2.2}$$

Figure 2.2 illustrates these terms for a wide range of passenger vehicles. At high velocities the aerodynamic drag is the largest resistive force, showing the importance of aerodynamics in terms of the energy consumption of vehicles.

It is well documented in the literature that for a passenger vehicle approximately 25% or more of the drag originates from the wheels [7, 8]. Therefore, knowledge of wheel aerodynamics is essential for creating aerodynamically efficient vehicles. However, the rotation and bluff-body geometry of the wheels result in complex flow fields that present challenges for both experimental and numerical methods. This is reflected in the number of publications concerning wheel aerodynamics, some of which will be presented in the coming section.

For clarity, it is noted that in this thesis, wheel is used as a general term, describing the combination of tyre and rim. Various features of the wheel are named in Figure 2.3.

2.2 Literature review

Many investigations have focused on the difference between stationary and rotating wheels [8–16]. Wäschle [9] presented the flow structures for the two cases and showed that there can be significant differences in drag depending on the rotation. Moreover, since the wheel rotation alters the flow field, optimisation of other components will be affected by the wheel state. Hence, rotating wheels are necessary not only for accurate absolute drag predictions but also for determining drag deltas between configurations. These interactions were further established by Wang et al. [10]. Using a simplified vehicle model, they showed how different wheel rotation states can alter the wake balance and the global forces. The largest differences were obtained between rotating and stationary rear wheels, resulting in a drag difference of 0.054 C_D.

Much of the work related to wheel aerodynamics has studied the impact of the rims, both in

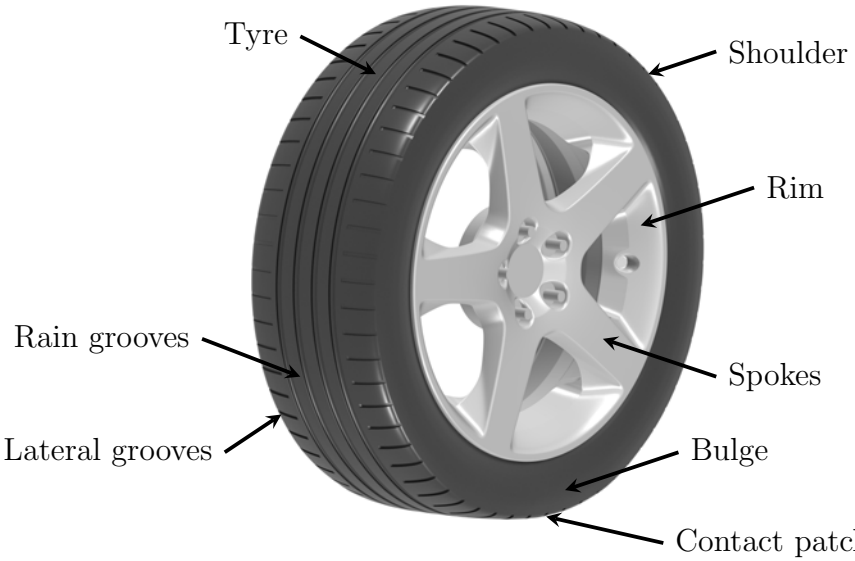

Figure 2.3: *Naming convention used for various features. Wheel is used to denote the combined tyre and rim system.*

terms of drag [17–22] and ventilation moment [8, 23–25]. Although this is of high importance for wheel flows, the main focus of this work is on the tyre, and the tyre in combination with the rim, rather than rim designs and modelling.

2.2.1 Tyre aerodynamics

Many studies have focused on isolated wheels [26–41]. Fackrell and Harvey [26] were among the first to investigate a rotating wheel, finding that the wheel rotation resulted in separation on top of the tyre further forward than in the stationary case. They also found that the pressure coefficient can exceed one at the contact patch. This was explained by the so-called jetting phenomena, where the rotation of the wheel adds energy to the flow. The jetting creates a pair of vortices at either side of the contact patch. The same was confirmed by Mears et al. [27], who also measured a strong negative pressure peak right downstream the contact patch. Later research, such as Croner et al. [28], have combined experimental and numerical techniques to confirm and further explain the flow structures of an isolated wheel.

The interaction between the wheels and the vehicle has been investigated on simplified vehicles, either by encapsulating isolated wheels in wheelhouses [8, 42, 43] or using scale models [7, 10, 44]. Although these works provide important insight into the flow physics, they lack some of the effects observed with a realistic vehicle. These effects have been considered in [9, 15, 45–47], where detailed production vehicles were used.

The geometry of the tyre can have a significant impact on the flow. For example, Wittmeier et al. [44] showed that both drag and lift are influenced by the tyre profile, especially at the outer shoulder. The geometry is also subject to deformations due to both static and dynamic loads. The importance of considering these deformations has been demonstrated in [40, 46–49].

Croner [50] studied the tread pattern on an isolated wheel and found that adding rain grooves reduces the jetting phenomena and injects momentum to the wake downstream of the tyre. Wang et al. [10] investigated, among other things, three tread patterns: slicks, rain grooves and rain grooves with a rough shoulder. It was found that the rain grooves reduced the drag and an additional drag reduction was found when combining the grooves and the rough tyre shoulder. Wang et al. [10] concluded that the various tyres resulted in changes of the same character, but in smaller magnitude, as those of comparing rotating and stationary wheels.

Tread patterns were added to more realistic geometries in Mercker et al. [15] who found that the drag was increased compared to a slick tyre. Wickern et al. [8] also investigated the effect of adding tread patterns to slick tyres and reported a drag reduction of 0.005 C_D for a closed rim but an increase of 0.002 C_D for an open rim. Similar results were observed by Hobeika and Sebben [45] when comparing slick and detailed tyres. The variance in results indicates the complexity of tyre aerodynamics, particularly when considering the interaction with the rims and vehicle geometry.

2.2.2 Numerical modelling of wheels

Performing numerical simulations of rotating wheels presents challenges regarding geometry replication and boundary conditions. As presented in Section 2.2.1, the flow is sensitive to the geometry of the tyre. This was illustrated by Diasinos et al. [31] who considered various simplifications in the CFD, concluding the importance of matching the geometry between experiments and simulations. Since the tyre is not a rigid body, the geometry replication is complicated as the tyre undergoes static deformation from the weight of the vehicle, creating the contact patch and sidewall bulge, and dynamic deformation due to the rotational forces. As shown by Landström et al. [47], the tyre expands radially and contracts axially. Additionally, depending on the suspension system and test setup, the wheel can move up into the wheelhouse or alter the ride height of the vehicle [51]. As illustrated by both Landström et al. [47] and Gray et al. [49], these deformations can be measured, but it requires additional care in comparison to, for example, using conventional 3D scanning of static tyres.

The simulation of the rotating boundary condition is complicated by the contact between the tyre and the ground, limiting which modelling techniques can be used since the tyre is non-circular. Although methods such as immersed boundary can model this type of rotation [32, 33], their high computational cost makes them unfeasible for use in vehicle development. Instead, the available methods typically consist of rotating wall, moving reference frame (MRF) and sliding mesh (SM). Among these, SM is the only method where the geometry actually rotates, making it the most physical option. However, SM requires a rotational symmetric interface to the surrounding region. Moreover, for features such as the bulge to remain in the same position, the use of SM would require the geometry to be deformed during the simulation, making it an unsuitable boundary condition for the tyre. Instead, SM is the preferred method for modelling the rim [21, 22, 39, 45, 52].

For smooth tyres, rotating wall, which applies a tangential velocity to the surface, is adequate. However, for tyre features where there is a need for a surface normal velocity, such as in lateral grooves, the method fails. Some studies have modelled the grooves using a surface roughness

[39]. However, such a method requires the roughness value to be tuned for every tyre. A better approach for modelling the lateral grooves is the MRFg method, presented by Hobeika and Sebben [45, 52]. There, MRF regions are used inside the grooves, adding rotational momentum without moving, and replicating the effect of the grooves [36, 53].

2.2.3 Wind tunnel interference

When performing tests in a wind tunnel the geometry of the tunnel will affect the results. Compared to open road conditions, the wind tunnel introduces differences in terms of blockage and moving ground simulation. Performing CFD in open road conditions, a negligible blockage of 0.5% or smaller is typically used [54], whereas the blockage in a wind tunnel is usually around $5 - 15\%$ [55]. In terms of ground simulation, open road CFD uses a fully moving ground, replicating the relative velocity between the air and ground obtained when driving on the road. In a full-scale wind tunnel designed for passenger vehicles, a five-belt system is commonly used, which has been shown to alter both drag and lift compared to a full moving belt [56].

Previous work on wheel aerodynamics has indicated that wheel flows could be sensitive to the differences between open road and the wind tunnel environment. For example, Hobeika and Sebben [45] and Koitrand et al. [22] identified that the experimental wind tunnel results of fully closed rims were difficult to replicate using open road CFD. Hobeika and Sebben [45] presented the hypothesis that some of the differences could be explained by interference effects of the wind tunnel.

To account for the interference Fischer et al. [57, 58] performed simulations including the geometry of an open jet wind tunnel and found that the predictions generally improved. Cyr et al. [59] compared different underbody configurations and concluded that including the wind tunnel generally improved the agreement to experiments. For a slotted wall tunnel, Ljungskog et al. [60] found that considering the wind tunnel geometry improved the prediction of absolute drag, whereas a less clear trend was observed for the prediction of configuration deltas. Moreover, Ljungskog et al. [60] reported that the largest differences between open road and wind tunnel simulations occurred in areas of strong acceleration, such as around the wheels, and between open and closed rims.

Few studies have compared open road and wind tunnel computations from the perspective of predicting wheel flows. Haag et al. [21] used a scale model DrivAer in an open jet wind tunnel with fully moving ground to study different rims. When comparing experiments and numerical simulations, where part of the wind tunnel geometry was modelled, the differences between the rims were well predicted. Although no open road simulations were performed, wind tunnel interference was observed from the mounting solution, where the struts holding the wheels altered the flow.

Another consideration when comparing wind tunnel experiments and CFD is the parasitic force acting on the wheel drive units (WDUs), as described in [60–62]. In a wind tunnel equipped with a five-belt system, WDUs are used to rotate the wheels and, to allow for lift measurements, these are connected to the underfloor balance. With this setup, a parasitic force, created by

the pressure acting on the WDUs, will be included in the lift measurements.

3

Methodology

3.1 Vehicle geometry

For the wind tunnel test, a full-scale model of the DrivAer reference vehicle, introduced by Heft et al. [63], was used. The specific test object was the Ford open cooling DrivAer, as described by Hupertz et al. [64, 65], featuring a simplified suspension system, rotating brake disks as well as a detailed engine bay and underbody. The model was tested in the notchback configuration with closed grilles, Figure 3.1. Additionally, a small airdam was fitted to simplify the underbody leading-edge separation, which has proven challenging to predict consistently in both experiments [65] and numerical simulations [66]. For the simulations with the wind tunnel geometry included, the rocker panel restraint posts used for mounting the vehicle in the wind tunnel are replicated, as shown in Figure 3.1a.

3.1.1 Tyres

The tyres were modified racing tyres with diameter 640 mm and width 218 mm. Four tread patterns were considered; slick (S), rain grooved (R), lateral grooved (L) and detailed (D), Figure 3.2. Apart from the tread pattern, the tyres were identical. Since the tyres were stiff racing tyres, the dynamic deformations, caused by the rotational forces, were small. This was demonstrated by Hobeika and Sebben [45], who approximated the rotational forces by considering large variations in inflation pressure and 3D scanning the tyres.

Although the dynamic deformation was small, the static deformation still had to be considered.

(a) *Side view* **(b)** *Front view*

Figure 3.1: *Vehicle geometry and coordinate system.*

(a) *Slick (S)* **(b)** *Rain (R)* **(c)** *Lateral (L)* **(d)** *Detailed (D)*

Figure 3.2: *Investigated tread patterns.*

(a) *Unloaded tyre* **(b)** *Loaded tyre* **(c)** *Plaster casting*

Figure 3.3: *Steps for 3D scanning the tyres.*

Therefore, a set of 3D scans were performed, capturing different aspects of the tyre geometry. Firstly, an unloaded tyre was scanned (Figure 3.3a), allowing recreating the undeformed tyre profile. Next, the tyres were scanned while mounted to the vehicle (Figure 3.3b), capturing the bulge above the contact patch. Due to limitations of the scanner and accessibility, the narrow gap between the tyre and the ground, as well as the inner bulge could not be captured in this setup. Hence, plaster castings of the bottom 30 mm of the tyre were performed and scanned, capturing the area around the contact patch, Figure 3.3c. Using the scans, the tyre was built and morphed in ANSA. The resulting deformation at the centreline of the front contact patch ($x = 0$) is shown in Figure 3.4.

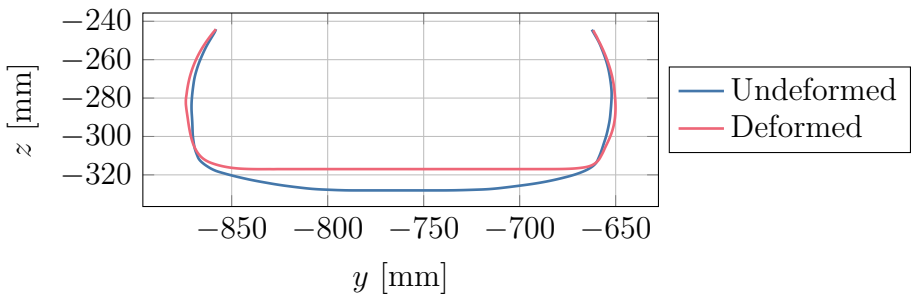

Figure 3.4: *Difference between the undeformed and deformed front right tyre at the wheel centreline ($x = 0$).*

(a) *Open rim (OR)* **(b)** *Closed rim (CR)*

Figure 3.5: *Investigated rim designs.*

3.1.2 Rims

The tyres were mounted on production rims. The rims were tested in two configurations, open and closed, Figure 3.5. For the closed configuration, a flat piece of sheet metal was attached to the outside surface of the rim.

3.2 Experimental setup

For the experiments, the Volvo Cars Aerodynamic Wind Tunnel (PVT), as described in detail by Sternéus et al. [67], was used. The wind tunnel has a slotted wall test section and a boundary layer control system, consisting of a scoop, distributed suction, a five-belt system and tangential blowers, Figure 3.6. For these investigations, the tangential blowers were deactivated, simplifying comparisons to numerical simulations.

3.2.1 Flow field measurements

Flow field measurements were performed using the traversing gear in the wind tunnel. Two 12-hole Omniprobes sampled the pressures, which were later used for calculating velocity components as well as static and dynamic pressure, using the calibration from the manufacturer. The accuracy of the probes was stated to be 3% for velocity magnitude, corresponding to 1 m/s in the freestream, and 1.5° for angularity [68].

The investigated planes are shown in Figure 3.7. At the front wheel, two x-normal planes, located at the front wheel axle ($x = 0$) and 400 mm further downstream, were used along with a y-normal plane at $y = 904$ mm. These planes were located such that the point closest to the vehicle was approximately 30 mm from the outermost point of the tyre bulge. Downstream the vehicle, a plane was placed at $x = 4000$ mm, corresponding to 200 mm behind the bumper.

The traverse introduces a disturbance in the flow. A study by Sterken et al. [69] showed that, for measurements behind the vehicle, the drag was altered by the traverse. To quantify the

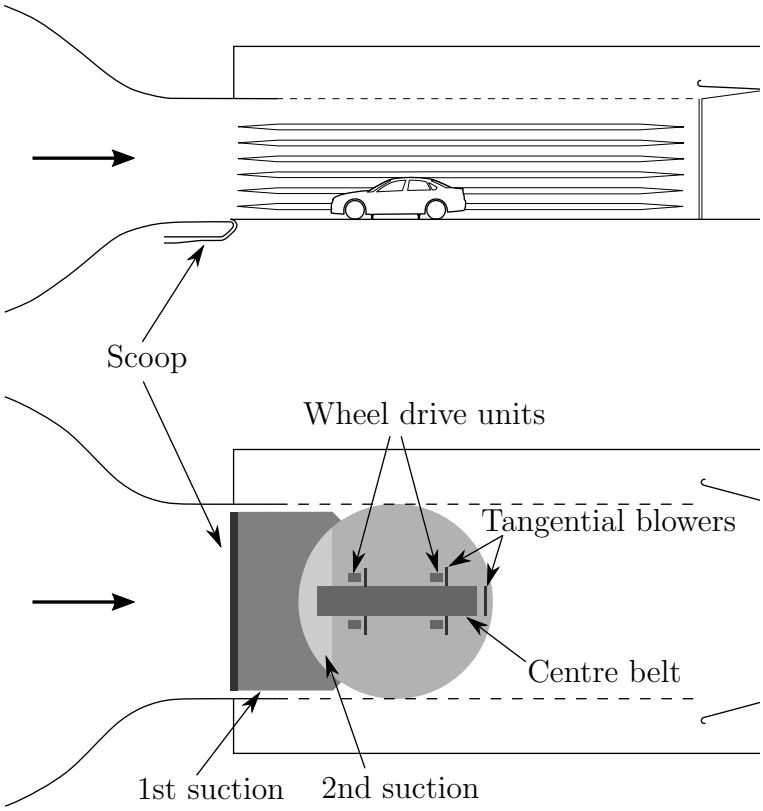

Figure 3.6: *Boundary layer control system in PVT drawn to scale. Adapted from [60].*

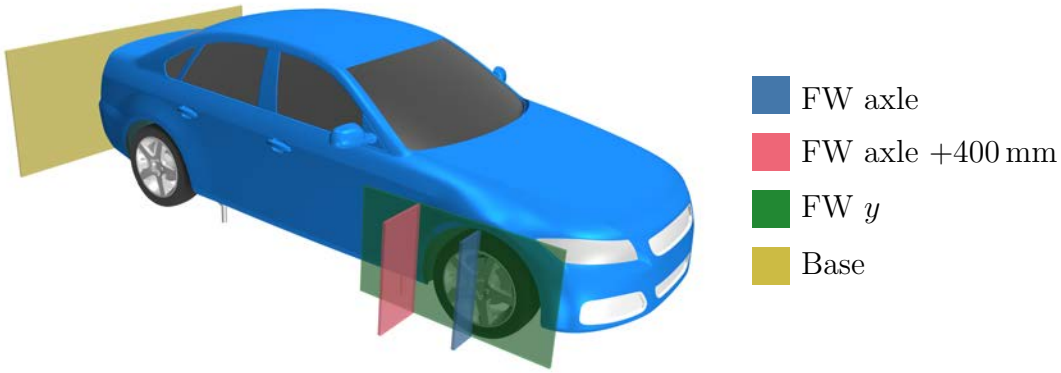

Figure 3.7: *Locations and names of the flow field measurement planes.*

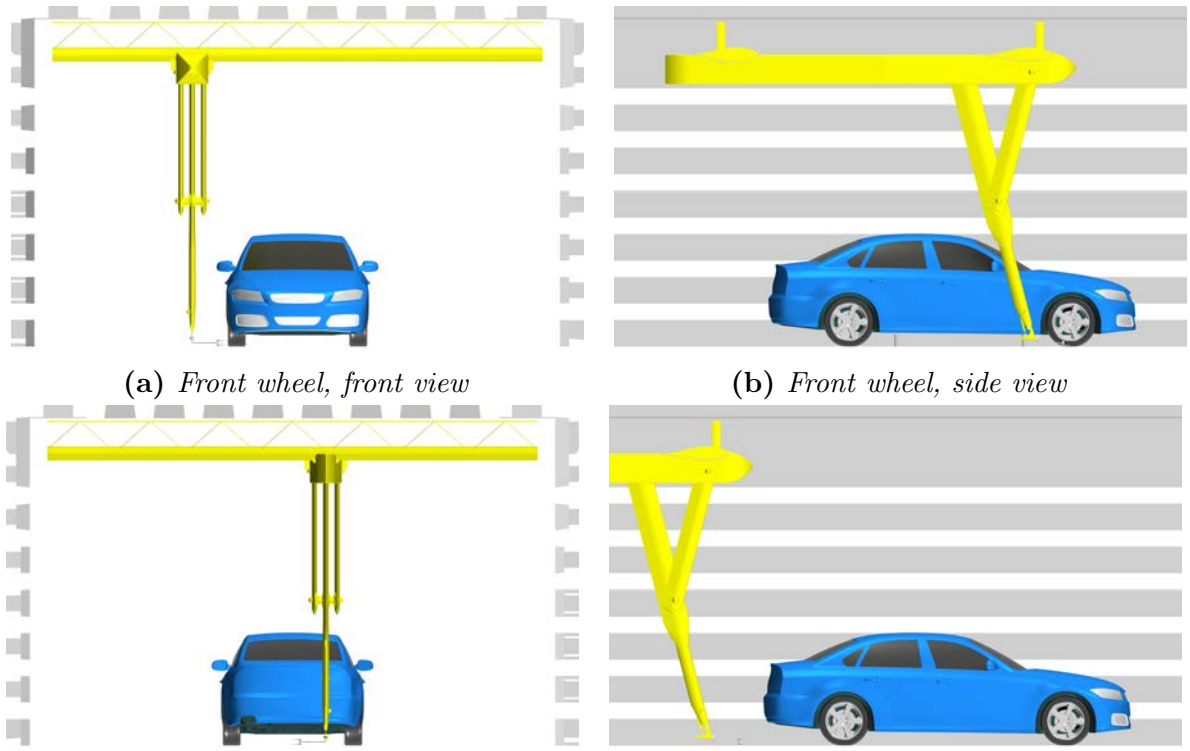

(a) *Front wheel, front view* **(b)** *Front wheel, side view*

(c) *Base, rear view* **(d)** *Base, side view*

Figure 3.8: *Positioning of the traverse for determining interference at the front wheel and in the base wake. The slotted walls of the wind tunnel are shown to indicate the size of the test section.*

effects in this work, numerical simulations where the traverse geometry was included were performed and compared to simulations without the traverse. These were performed with the rain grooved tyre and the open rim. Two traverse placements were studied, one at the front wheel and one in the base wake, Figure 3.8. In both cases the traverse was placed in its lowest position as this was believed to result in the largest flow disturbance. The placement at the front wheel corresponded to the intersection between the planes FW axle and FW y and in the base wake the probes were located in $y = 0$. Including the traverse, some differences were observed both at the front wheel and in the base wake, Figures 3.9 and 3.10. However, overall the flow structures were similar, especially close to the probe location. Therefore it is assumed that the measurement technique allows for comparisons between experiments and simulations.

3.2.2 Pressure measurements

The test object was equipped with a pressure measurement system, as described by Hupertz et al. [65]. In particular, the front left wheelhouse was equipped with two rows of pressure taps, each located along a constant y cross-section. In this work, the pressures at the innermost row ($y = -600\,\text{mm}$) are presented. Due to the construction of the traverse, the pressure and flow field measurements were performed at opposite sides of the vehicle. However, since the DrivAer is symmetric upstream the end of the front wheelhouses, the differences between the sides should be minimal.

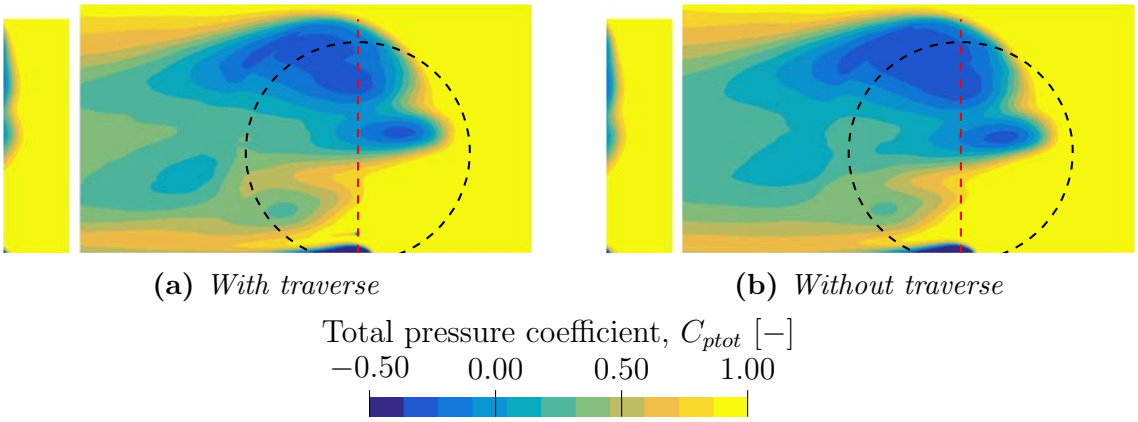

(a) *With traverse* **(b)** *Without traverse*

Figure 3.9: *Total pressure coefficient from CFD in the planes FW axle and FW y. The traverse was positioned according to Figures 3.8a and 3.8b. The lines mark the outline of the tyre and the location of the FW axle plane.*

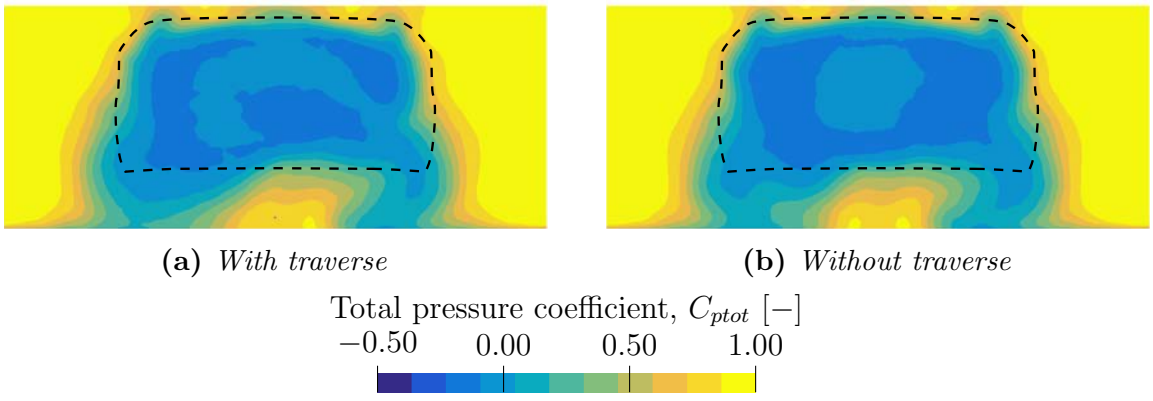

(a) *With traverse* **(b)** *Without traverse*

Figure 3.10: *Total pressure coefficient from CFD in the base plane. The traverse was positioned according to Figures 3.8c and 3.8d. The dashed line marks the outline of the vehicle base.*

3.2.3 Blockage correction

The blockage corrected drag was used to enable comparisons between forces from wind tunnel experiments and open road simulations. The corrected value was calculated as

$$C_{D,\text{corr}} = \frac{C_{D,\text{uncorr}} + \Delta C_{D,\text{HB}_\text{TS}}}{(1+\varepsilon_s+\varepsilon_w)^2} + \Delta C_{D,\text{HB}_\text{model}}, \tag{3.1}$$

where the dynamic pressure was corrected for solid body displacement, ε_s, and wake blockage, ε_w, calculated as

$$\varepsilon_s = \tau\sqrt{\frac{V}{L}}\frac{A}{A_\text{TS}^{3/2}}, \quad \varepsilon_w = \frac{A}{A_\text{TS}}\left(\frac{C_{D,\text{uncorr}}}{4}+\eta\right). \tag{3.2}$$

Here, the vehicle volume V, length L and frontal area A were used along with the cross-sectional area of the test section A_TS and constants τ and η.

In Equation (3.1), corrections were also applied for horizontal buoyancy. Firstly, the horizontal buoyancy of the empty test section, which was calculated from measurements of the empty test section pressure gradient, was considered through $\Delta C_{D,\text{HB}_\text{TS}}$. Secondly, $\Delta C_{D,\text{HB}_\text{model}}$, which was based on empirical data, corrected for the horizontal buoyancy induced by the model. A detailed description of the correction method and its derivation was presented by Eng and Walker [70].

Inserting the properties of the DrivAer notchback ($V = 6.58\,\text{m}^3$, $A = 2.17\,\text{m}^2$, $L = 4.61\,\text{m}$) and the range of drag values considered in this work, the correction was approximately $C_{D,\text{corr}} \approx 0.936 C_{D,\text{uncorr}}$.

3.3 Numerical setup

All numerical simulations were performed in Star-CCM+. An unsteady setup was used, employing the Improved Delayed Detached Eddy Simulation (IDDES) model and using the SST k-ω model in the URANS regions. All variables were discretised with the hybrid second-order upwind/bounded central differencing scheme in space and with an implicit second-order scheme in time.

3.3.1 Computational domains

Two computational domains were considered, representing open road and wind tunnel conditions. For open road, a rectangular domain, measuring $70 \times 40 \times 30\,\text{m}$, was used, Figure 3.11a. The vehicle was placed 20 m from the inlet. A uniform inlet velocity of 140 km/h was prescribed along with a pressure outlet with a gauge pressure of 0 Pa. For the ground, which was modelled as a moving wall, the same velocity as at the inlet was used, resulting in the desired relative velocity between the vehicle and the ground. The sides and top of the domain used a zero-gradient condition.

When including the wind tunnel geometry in the simulations a detailed model of PVT was used, Figure 3.11b. The model consisted of the high-speed leg of the wind tunnel, starting at

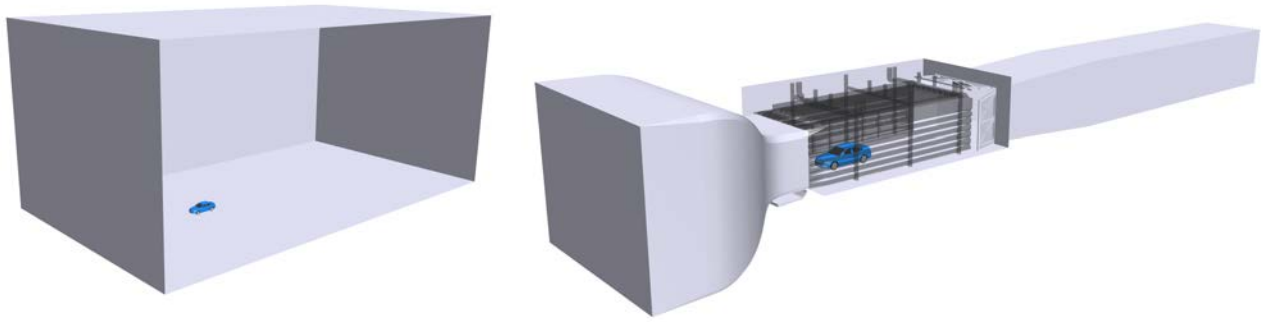

(a) *Open road domain* **(b)** *Wind tunnel domain (PVT)*

Figure 3.11: *Computational domains used for the numerical studies. Note that the domains are not shown in the same scale.*

the settling chamber, through the test section, to an extension of the diffuser. At the inlet a uniform mass flow was prescribed, and the outlet used a constant pressure of 0 Pa. Using the same method as in the physical wind tunnel, the mass flow was tuned to result in a test section velocity of 140 km/h. By considering the pressure drop over the nozzle, ΔP, the reference velocity was given by

$$U_\infty = \sqrt{\frac{2k_q \Delta P}{\rho}}, \tag{3.3}$$

where k_q is a calibration coefficient from the commissioning of PVT and ρ is the air density. Furthermore, since a constant pressure of 0 Pa was set at the outlet, downstream of the diffuser, negative pressure was obtained in the test section. Using the same method as in the physical tunnel, the reference pressure was calculated as

$$P_\infty = P_{C2} + k_p \Delta P. \tag{3.4}$$

Here, P_{C2} is the pressure at the nozzle exit and k_p is another calibration coefficient. For simulations with the wind tunnel geometry, U_∞ and P_∞ were used for the non-dimensionalisation of forces and pressures. For open road simulations, the reference velocity and pressure were taken as the inlet velocity (140 km/h) and outlet pressure (0 Pa), respectively.

For the wind tunnel simulations, the full boundary layer control system was modelled using the same method as described by Ljungskog et al. [60]. Starting with the scoop, part of its geometry was replicated, followed by a boundary condition specifying the outgoing mass flow. Next, the two distributed suction zones were modelled as slip walls in the tangential direction and with a specified velocity in the wall-normal direction. The air extracted by the scoop and the suction zones was reinjected outside of the slotted walls, corresponding to the setup in the physical wind tunnel. The five belts used a moving wall condition. The tangential blowers were omitted from the simulations since they were not used during the physical wind tunnel campaign.

3.3.2 Mesh

The mesh was hexahedral dominant with prism layers on all no-slip walls. At the external vehicle surfaces a low y^+ approach was employed, using 12 prism layers and resulting in $y^+ < 1$.

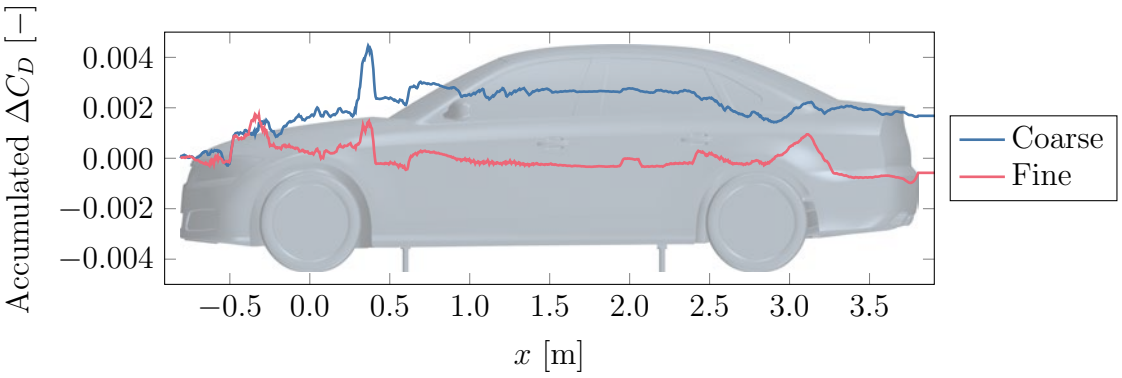

Figure 3.12: *Accumulated ΔC_D for different mesh sizes compared to the mesh used in the study.*

To establish the mesh sensitivity, various mesh sizes were considered. For these investigations, the setup with the wind tunnel geometry was considered since the mesh for this case was more challenging to build. From the baseline mesh, consisting of 223 million cells, comparisons were made with both a coarser (175 million cells) and a finer mesh (294 million cells). These were constructed by altering the bulk mesh, leaving the height of the prism layers unchanged. Figure 3.12 shows the accumulated drag, compared to the baseline. Although some differences were observed, most notably at the end of the front wheelhouse, these were small. For the fine mesh, the maximum and overall deviations were 0.002 and 0.0005 ΔC_D, respectively.

In addition to the mesh convergence, the mesh resolution was evaluated using the two-point correlation of the streamwise velocity, v_x, along the lines in Figure 3.13. The lines downstream of the vehicle were located along the car centreline ($y = 0$), whereas the lines downstream the wheels were located at the centreline of the right-hand side wheels ($y = 750\,\mathrm{mm}$). For a variable ξ, which can be divided into its mean and fluctuating component as $\xi = \overline{\xi} + \xi'$, the normalised two-point correlation is calculated as

$$C_\xi^{\mathrm{norm}}\left(\vec{x}_A, \vec{x}_B\right) = \frac{\overline{\xi'\left(\vec{x}_A\right)\xi'\left(\vec{x}_B\right)}}{\xi'_{\mathrm{RMS}}\left(\vec{x}_A\right)\xi'_{\mathrm{RMS}}\left(\vec{x}_B\right)}, \quad \xi'_{\mathrm{RMS}}\left(\vec{x}\right) = \overline{\xi'\left(\vec{x}\right)^2}^{1/2}, \tag{3.5}$$

where $\vec{x}_A$ and $\vec{x}_B$ are spatial coordinates. Davidson [71] showed that examining the two-point correlation gives a better indication of the resolution, compared to considering the fraction of resolved turbulent kinetic energy. Furthermore, Davidson [71] recommended that the largest eddies should be resolved by at least eight cells, corresponding to a correlation larger than zero for minimum eight cells. This criterion was fulfilled for all four lines, Figure 3.14.

Finally, the IDDES blending function was investigated, Figure 3.15. Away from the boundaries, LES was used and approaching the wall the switch to URANS occurred, as desired.

Overall, the baseline mesh (Figure 3.13) was considered sufficient. In the open road setup, the same mesh strategy and refinements were implemented, resulting in a mesh consisting of 165 million cells.

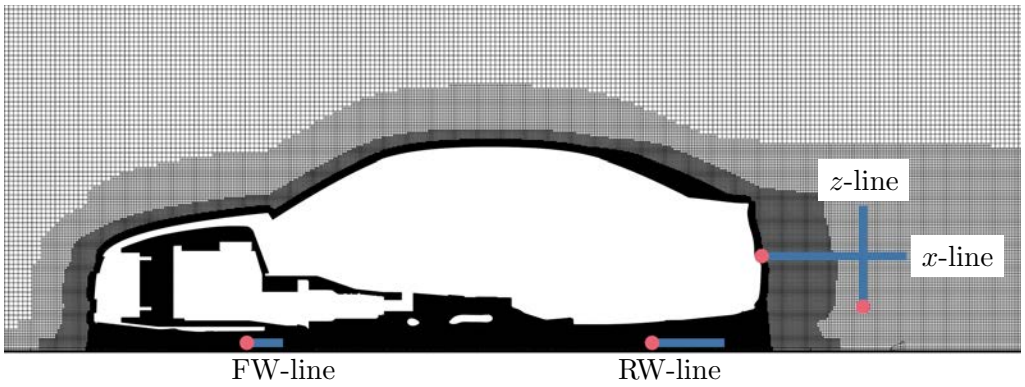

Figure 3.13: *Mesh along the centreline ($y = 0$) and the lines for two-point correlation. The red markers indicate the start of the sampling lines.*

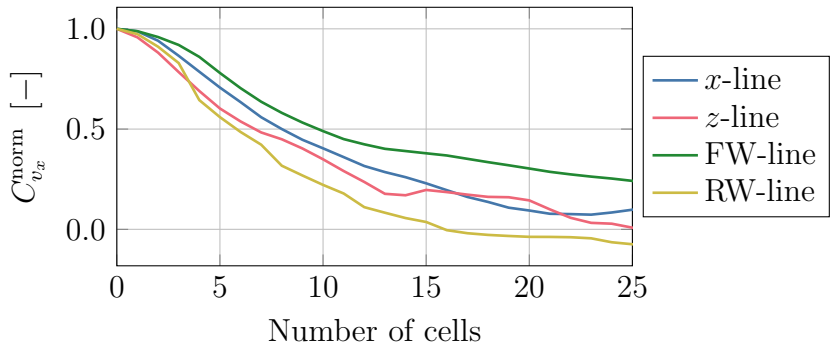

Figure 3.14: *Two-point correlation of the streamwise velocity along the lines illustrated in Figure 3.13.*

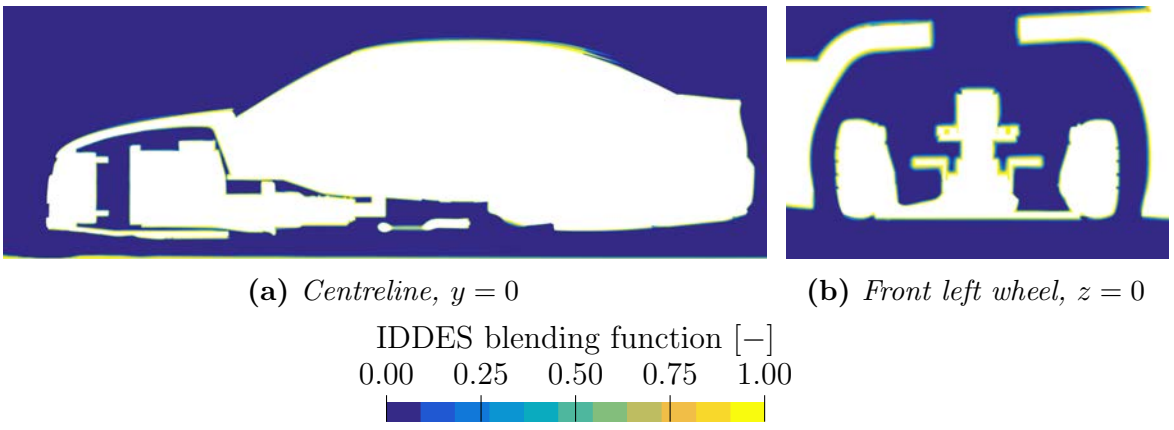

(a) *Centreline, $y = 0$* **(b)** *Front left wheel, $z = 0$*

Figure 3.15: *Blending function of IDDES showing regions of LES (zero) and URANS (one).*

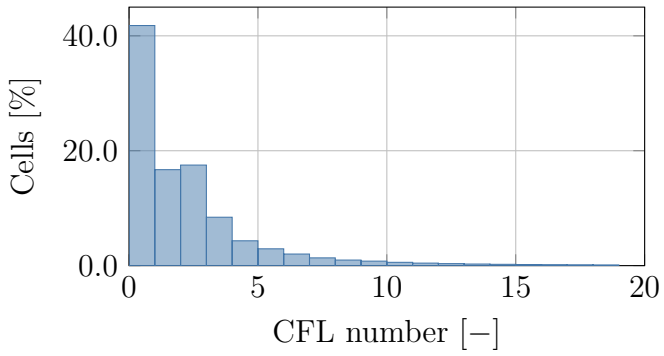

Figure 3.16: *Distribution of CFL number for the cells in the domain.*

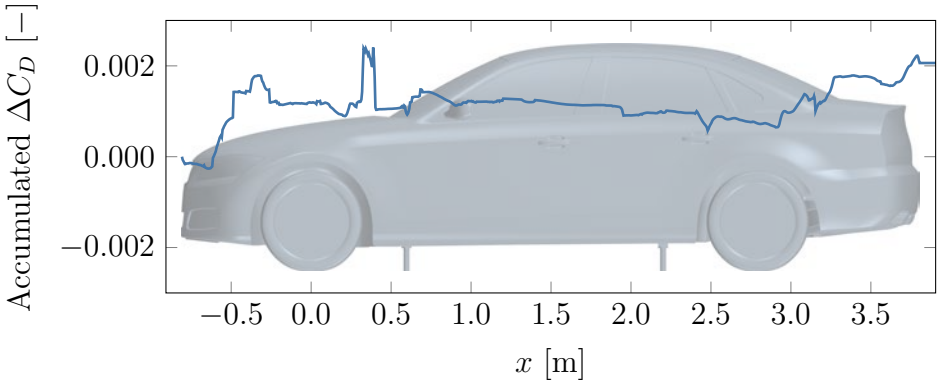

Figure 3.17: *Accumulated* ΔC_D *for a time step of* 1.25×10^{-4} s *compared to* 2.5×10^{-4} s.

3.3.3 Time step and averaging time

The simulations were started by computing a steady-state RANS solution. Next, the unsteady IDDES method was activated, initially using a coarse time step, which was lowered in steps until reaching the final value of 2.5×10^{-4} s. Once the flow had stabilised at this time step, the averaging was started.

The time-step was chosen such that a CFL number of approximately one was obtained in most of the domain. Ekman et al. [72] showed that accurate results could be obtained for CFL numbers of 20, which is significantly larger than in this work, Figure 3.16. The sufficiency of the chosen time step was further established by considering a smaller time step of 1.25×10^{-4} s. As shown in Figure 3.17, only small differences occurred compared to the baseline, with a maximum deviation of 0.002 ΔC_D.

The solution was averaged for 2 s, corresponding to 17 flow passages over the car. Figure 3.18 illustrates the instantaneous and running average of C_D for both open road and wind tunnel conditions. Using an averaging time of 2 s allows the running average to converge to within 0.001 C_D in both domains.

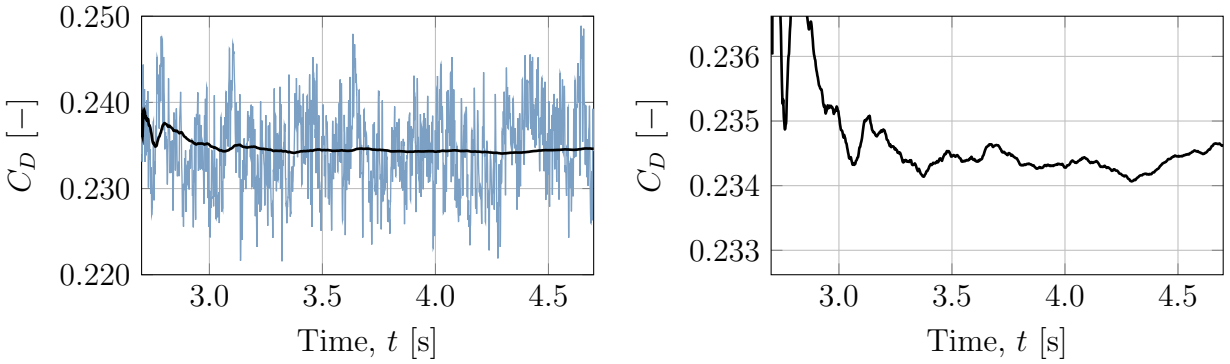

(a) *CFD open road*

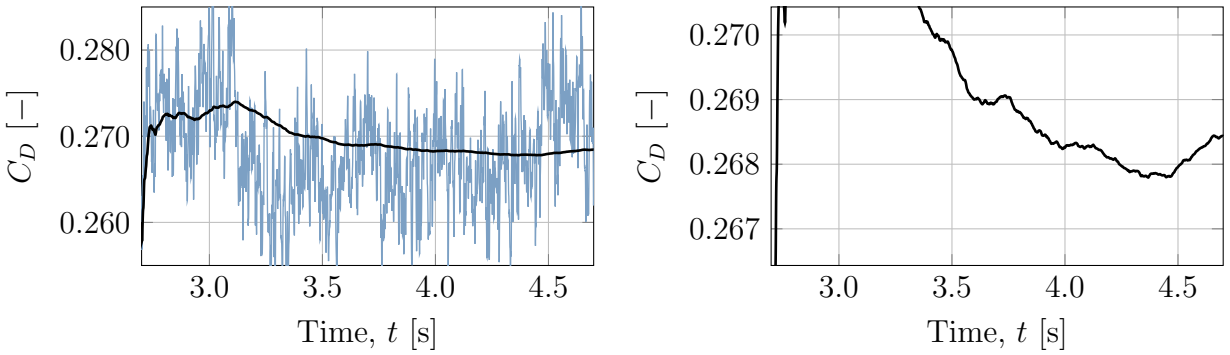

(b) *CFD PVT*

Figure 3.18: *Instantaneous (blue) and running average (black) of C_D for CFD open road and CFD PVT. The averaging starts at $t = 2.7\,\mathrm{s}$.*

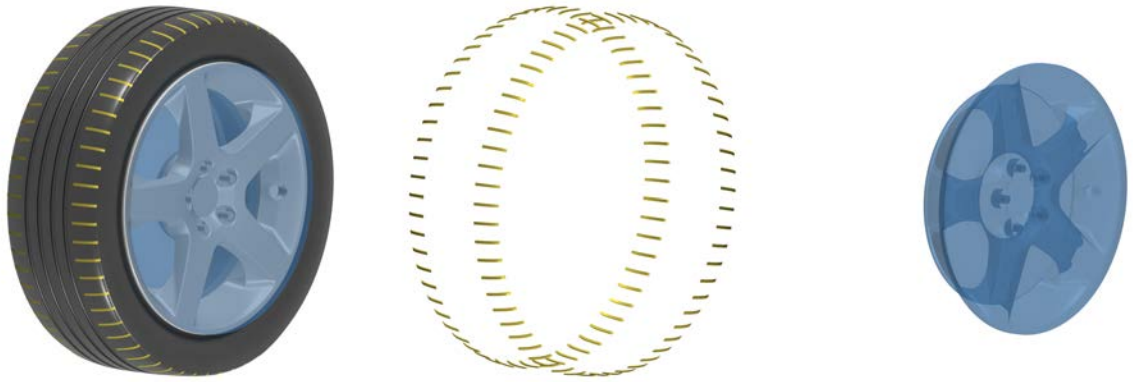

(a) *Complete wheel* **(b)** *MRFg regions* **(c)** *Sliding mesh region (SM)*

Figure 3.19: *Regions and surfaces of the wheel coloured by boundary condition.*

3.3.4 Wheel modelling

The Moving Reference Frame - grooves (MRFg) method, as proposed by Hobeika and Sebben [45, 52], was used to model the wheels. The rim was modelled with a sliding mesh (SM) and the tyre, except for the lateral grooves, used the rotating wall boundary condition, allowing deformed tyres to be used. In the lateral grooves, Moving Reference Frames (MRF) were used since rotating wall cannot replicate the motion of the grooves. The regions are shown in Figure 3.19.

3.3.5 Lift on wheel drive units

To account for the parasitic lift forces explained in Section 2.2.3, the pressure was integrated over the WDUs and the resulting force was added to the lift of the vehicle. Data where the WDU lift was included are denoted CFD WDU, as compared to CFD which included only the force on the vehicle.

3.4 Uncertainty of forces

To distinguish between significant and insignificant force differences, there is a need for establishing the uncertainty of the results, both for experiments and numerical simulations. For experiments, the in-test repeatability of the wind tunnel, as presented by Ljungskog et al. [60], was used. In the case of the simulations, multiple factors affected the uncertainty. Here, estimates based on observations and analysis during the validation of the methodology were used. These included the variations within the mesh study, time step study and from the averaging time. The uncertainties for the various force coefficients with the two methods are presented in Table 3.1. When considering deltas, the uncertainties were propagated, resulting in scaling by $\sqrt{2}$.

Table 3.1: *Force coefficient uncertainty for experiments, based on the wind tunnel repeatability, and corresponding estimations for the numerical simulations.*

Force	Coefficient	Uncertainty	
		Exp	CFD
Drag	C_D	±0.001	±0.002
Front lift	C_{LF}	±0.001	±0.002
Rear lift	C_{LR}	±0.005	±0.004

4

Wind tunnel interference and wheel aerodynamics

Most commonly, numerical simulations for external aerodynamics are performed in an open road setup, using a large computational domain with negligible blockage and a fully moving ground plane. These conditions differ from those of the wind tunnel, where the blockage is non-negligible and a fully moving ground is rarely used. Hence, results from experiments and CFD are not directly comparable. To obtain corresponding results, the wind tunnel data can be corrected for blockage, where a correction is applied to the forces measured by the wind tunnel balance. However, such a correction does not consider local changes in the flow field. Alternatively, the geometry of the wind tunnel can be included in CFD, enabling comparisons to uncorrected experimental data.

The aim of this study is to investigate how the wind tunnel influences the results, focusing on wheel aerodynamics, and to determine whether it is needed to include the wind tunnel domain in the numerical simulations to accurately replicate experimental data. The impact on absolute drag and a detailed examination of the flow around the wheels in the two domains are presented and discussed.

4.1 Absolute drag prediction

The absolute drag coefficient for the various tyre and rim configurations is presented in Figure 4.1. For the experiments, both blockage corrected and uncorrected values are shown. The uncorrected data is compared to the simulations with the wind tunnel geometry (CFD PVT) and the corrected data to CFD open road. The drag prediction is typically improved by including the wind tunnel geometry in the simulations. Comparing corrected experiments and open road CFD, the average absolute difference is 0.005 C_D, as compared to 0.002 C_D between uncorrected experiments and CFD PVT. Most notably, there is a significant discrepancy between corrected experiments and CFD open road for the slick and rain grooved tyres (S and R) on the closed rim, indicating that some flow features present in the wind tunnel do not occur for open road conditions.

4.2 Comparison of different tyres

During vehicle development, accurate estimations of the drag deltas between configurations can be more important than the absolute values. Therefore, the drag difference, ΔC_D, between tyres is examined. Figure 4.2 shows ΔC_D for the various tyres and rims obtained from the

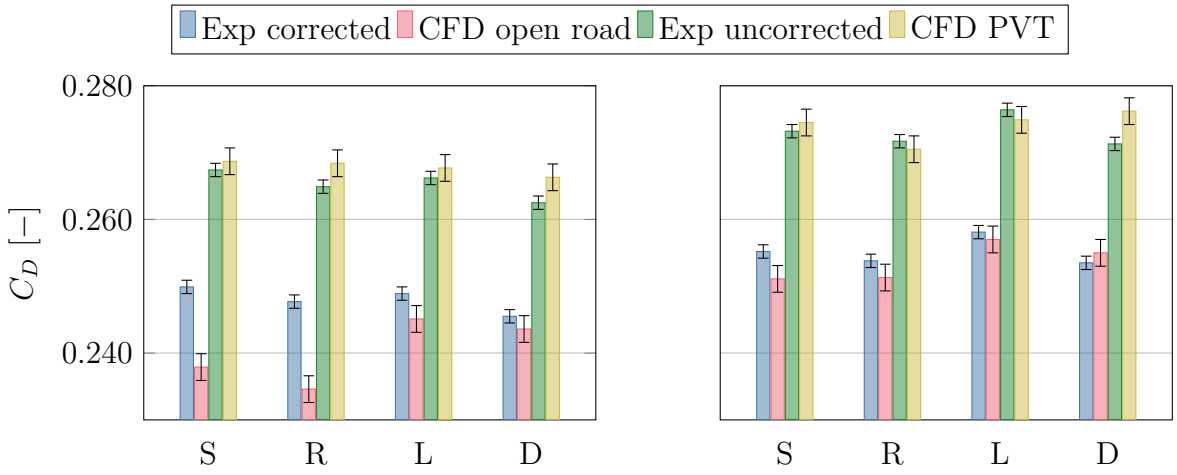

(a) *Closed rim* **(b)** *Open rim*

Figure 4.1: *Drag coefficient for the four sets of tyres: slick (S), rain grooves (R), lateral grooves (L) and detailed (D). Values from corrected and uncorrected experiments as well as numerical simulations with and without the wind tunnel geometry.*

different methods, using the slick tyre as the reference. Including the wind tunnel, the deltas are calculated to within the margin of uncertainty for all configurations. Excluding the wind tunnel, good agreement is found for some configurations, such as the rain grooved tyre (R) on both rims. However, for the deltas to tyres with lateral grooves (L and D), CFD open road mostly does not replicate the corrected wind tunnel results.

The accumulated ΔC_D for the various tyres on the two rims is shown in Figure 4.3. For the closed rim (Figure 4.3a), the rain grooved tyre gives similar differences to the slick for both CFD open road and CFD PVT. However, for the lateral grooved and detailed tyres, a significant difference is observed at the rear wheels and further downstream, where a drag increase occurs, causing the discrepancy in ΔC_D between the domains. For the open rim, the variations in accumulated ΔC_D are larger (Figure 4.3b), indicating a greater interaction between the flow around the tyre and the flow through the rim openings. Like the closed rim, the largest differences between the domains can be found at the rear wheels, where the lateral grooved and detailed tyres experience increased drag for CFD open road.

The difference in accumulated ΔC_D at the rear wheels can be explained by examining the separation around the rear tyre contact patch. Figure 4.4 shows the total pressure coefficient, C_{ptot}, at the right rear wheel in the plane $z = -300\,\text{mm}$ (17 mm above the ground). The field is illustrated for the various tyres on the closed rim, however, the same phenomenon occurs with the open rim. Examining the separation at the inner shoulder, similar results are observed for all tyres in CFD PVT. For CFD open road, a difference in both size and angle of the separation is seen, most notably when comparing tyres with (L and D) and without (S and R) lateral grooves. The inconsistencies between the domains are believed to be a result of the interaction between the front and rear wheels. As can be observed in Figure 4.4, the total pressure upstream of the rear wheels is lower in PVT than in open road. Examining a larger part of the same plane, Figure 4.5, the front wheel wakes are larger in CFD PVT than in CFD open road. Since a five-belt system is used in PVT, there is no moving ground between the

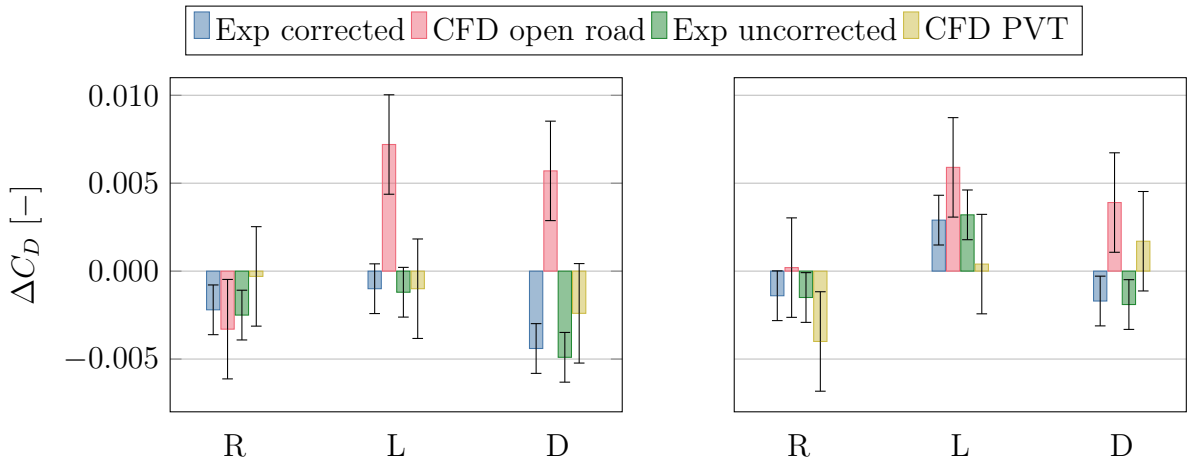

(a) *Closed rim* **(b)** *Open rim*

Figure 4.2: *ΔC_D for the different tyres compared to the slick. Data from experiments (corrected and uncorrected) and simulations (open road and PVT).*

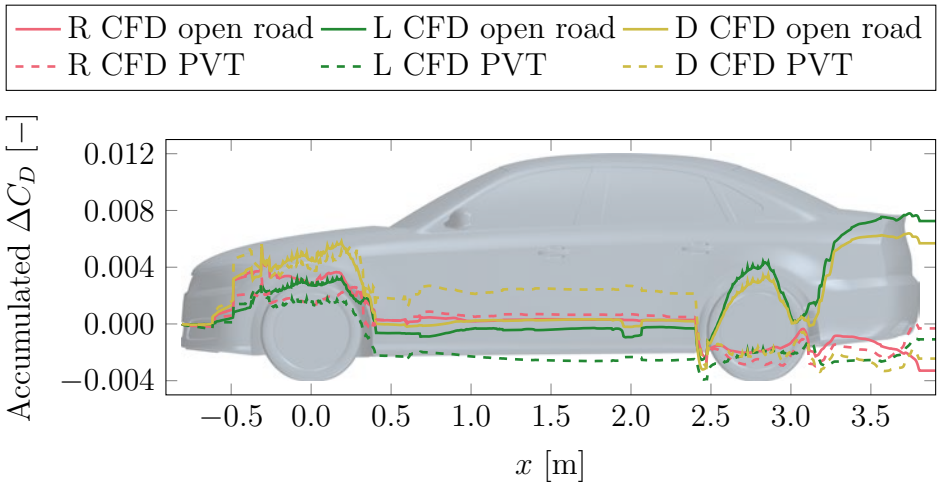

(a) *Closed rim*

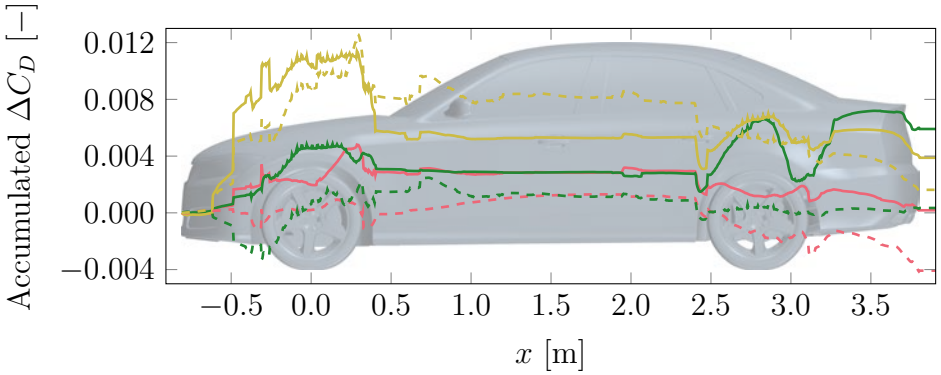

(b) *Open rim*

Figure 4.3: *Accumulated ΔC_D in open road and PVT for the two rims. The reference is the slick tyre.*

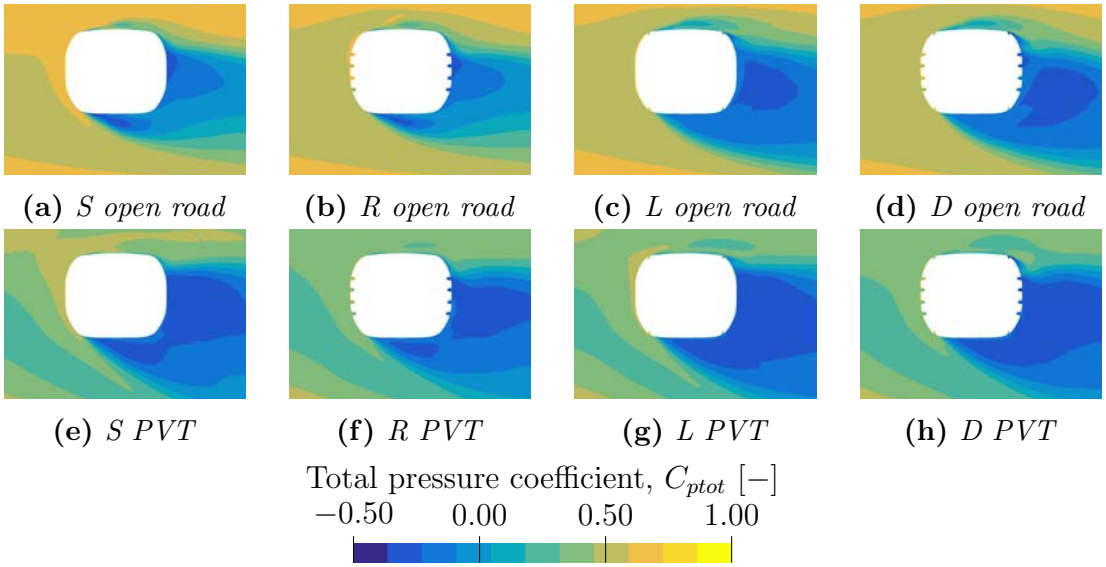

(a) *S open road* **(b)** *R open road* **(c)** *L open road* **(d)** *D open road*

(e) *S PVT* **(f)** *R PVT* **(g)** *L PVT* **(h)** *D PVT*

Figure 4.4: *Total pressure coefficient at the rear right wheel* 17 mm *above the ground for the closed rim in CFD open road and CFD PVT.*

front and rear wheels. The larger front wheel wakes shield the rear wheels to a greater extent, altering the sensitivity to separations from the lateral grooves. Hence, similar separation is obtained for all tyres in CFD PVT, whereas large differences are observed in CFD open road.

4.3 Comparison of different rims

Figure 4.6 presents the ΔC_D between open and closed rims obtained from the different methods. Generally, including the wind tunnel in CFD improves the agreement between simulations and experiments, in particular for the slick and rain grooved tyres. For the lateral grooved and detailed tyres, the delta is within the uncertainty for both domains.

The accumulated ΔC_D between open and closed rims is plotted for the slick tyre in the two domains, Figure 4.7. Some variation between the domains, believed to be caused by the difference in blockage, is observed at the front wheel. However, the largest discrepancies occur at the rear wheels and base. Examining the base wake for the rims in the two domains and comparing to experiments (Figure 4.8), a difference in width is noted between CFD open road and CFD PVT. For CFD PVT, the overall width is similar for both rims, aligning well with the experiments. However, for CFD open road, a distinct change in width is found between the closed and open rims, explaining part of the drag difference. These variations are believed to be caused by the increased blockage in PVT compared to open road.

4.4 Summary

To get an overview of the results the $\Delta\Delta C_D$, defined as

$$\Delta\Delta C_{D,\mathrm{x}} = \Delta C_{D,\mathrm{x,CFD}} - \Delta C_{D,\mathrm{x,exp}} = \left(C_{D,\mathrm{x}} - C_{D,\mathrm{S\text{-}CR}}\right)_{\mathrm{CFD}} - \left(C_{D,\mathrm{x}} - C_{D,\mathrm{S\text{-}CR}}\right)_{\mathrm{exp}}, \qquad (4.1)$$

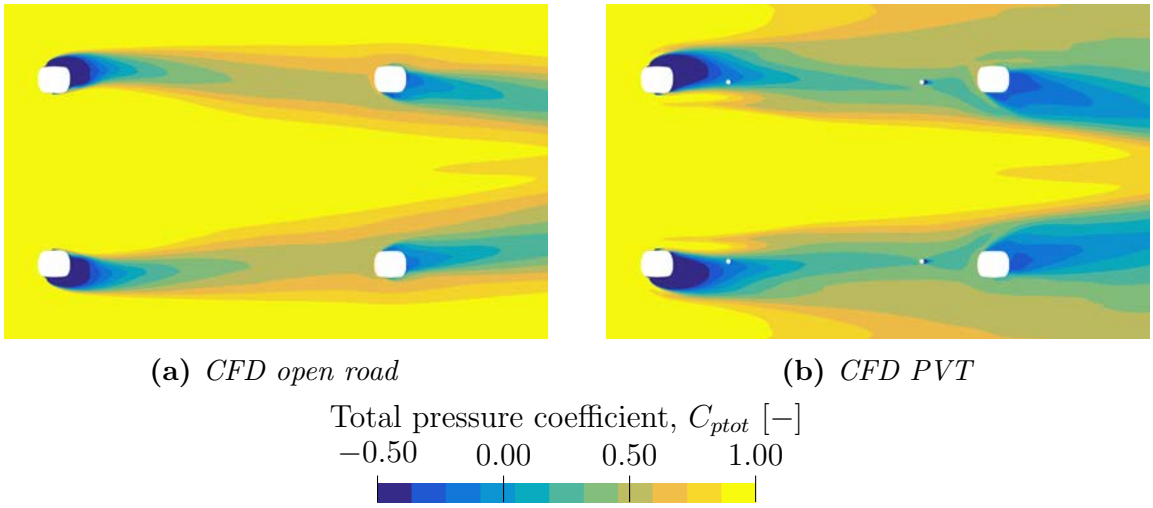

(a) *CFD open road* **(b)** *CFD PVT*

Figure 4.5: *Total pressure coefficient* 17 mm *above the ground for the slick tyre with closed rim.*

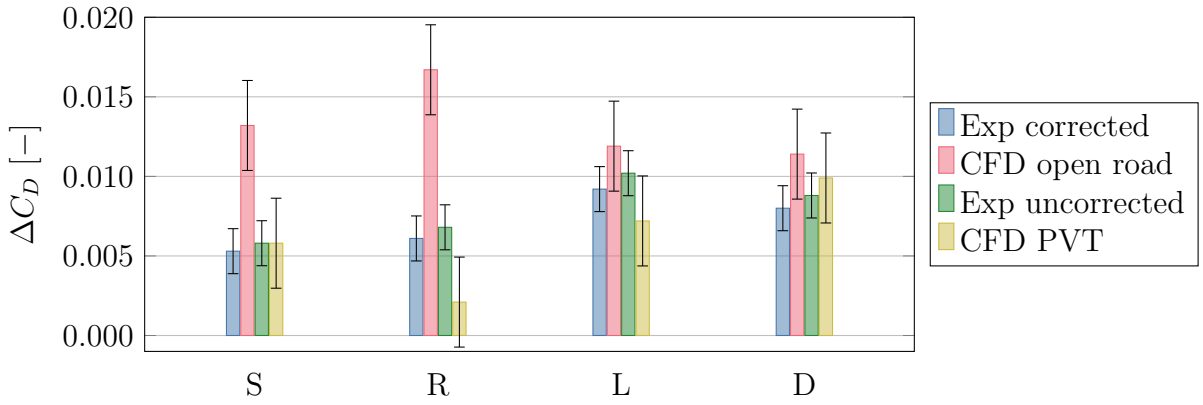

Figure 4.6: ΔC_D *between open and closed rims for the four tyres from experiments and simulations.*

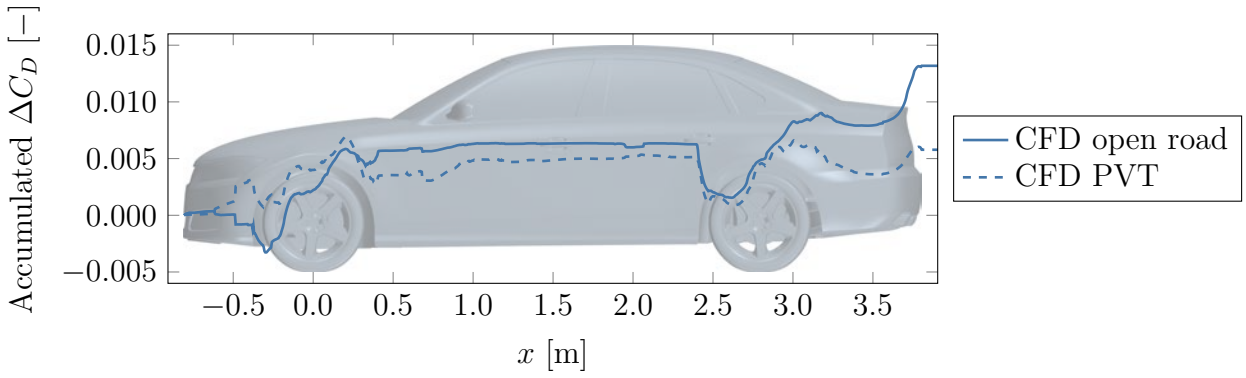

Figure 4.7: *Accumulated* ΔC_D *between open and closed rims for the slick tyre in open road and PVT.*

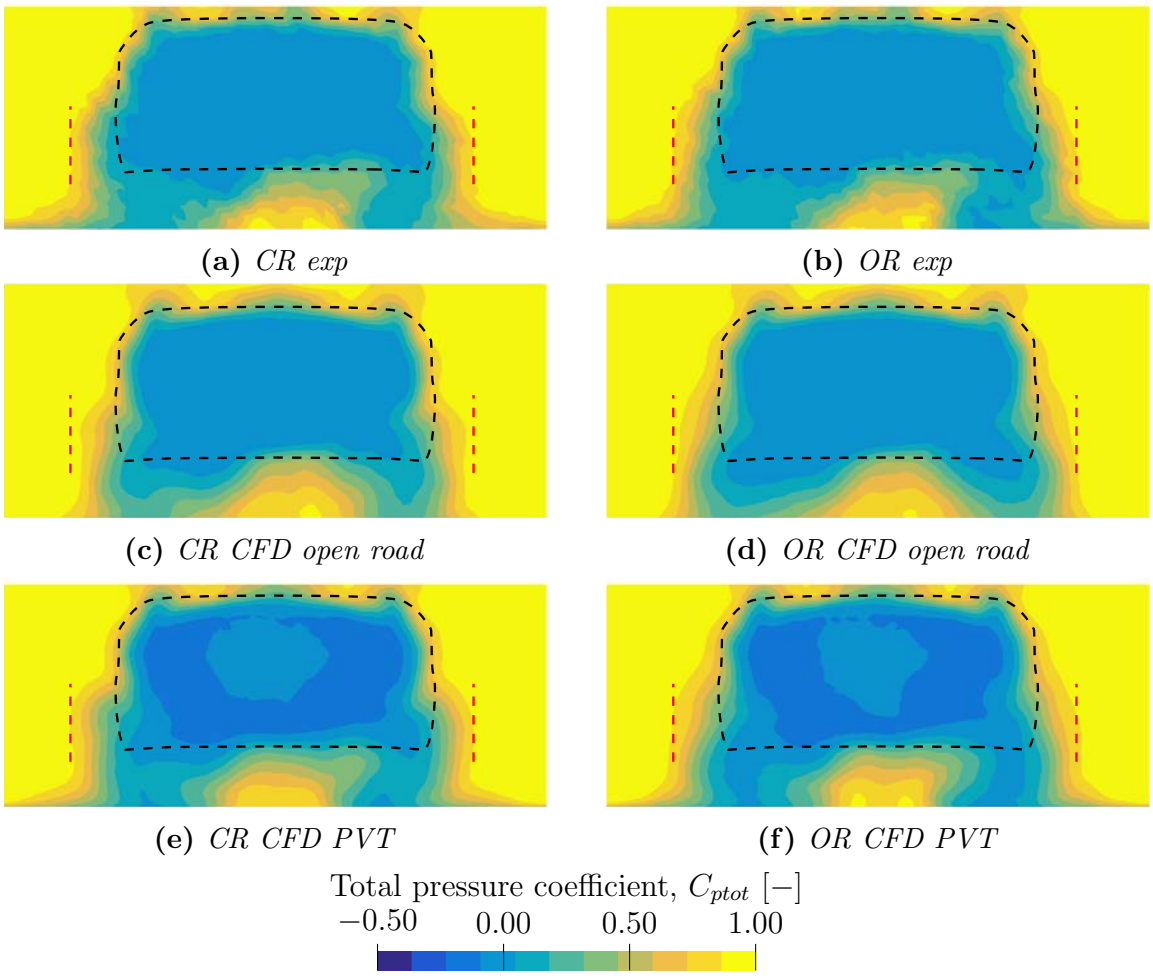

Figure 4.8: *Total pressure coefficient for the slick tyre with open and closed rims in the base plane. The results are shown for experiments, CFD open road and CFD PVT. The dashed black line marks the outline of the vehicle base and the dashed red lines are meant to assist in assessing the separation width. The lines are placed identically for all cases.*

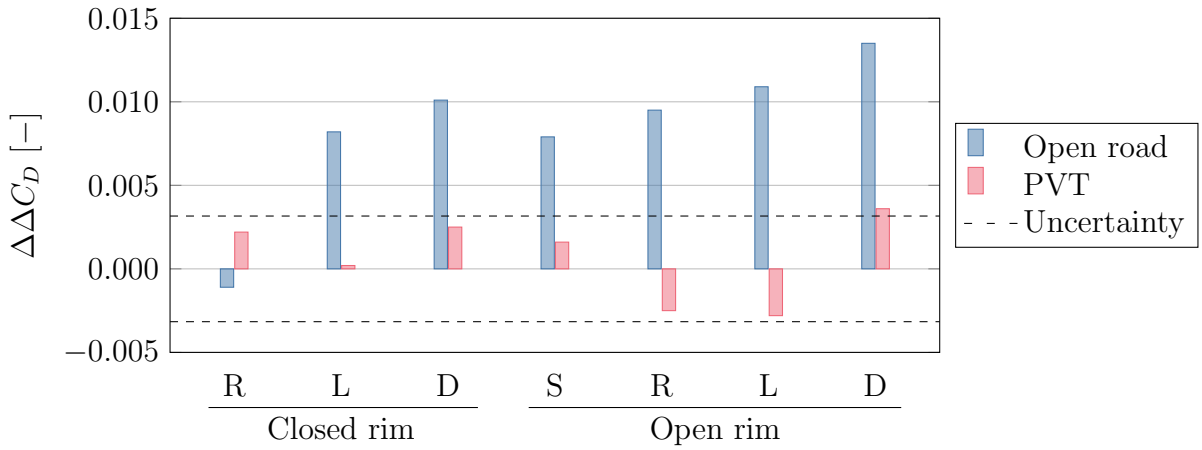

Figure 4.9: $\Delta\Delta C_D$, *as defined in Equation* (4.1)*, indicating the difference between open road (CFD open road and corrected experiments) and PVT (CFD PVT and uncorrected experiments) conditions. The slick tyre with closed rim is the reference.*

is considered. In the definition, x indicates the configuration investigated and S-CR is the slick tyre with closed rim, which is used as the reference. Figure 4.9 shows the $\Delta\Delta C_D$ for open road (comparing CFD open road to corrected experiments) and PVT (comparing CFD PVT to uncorrected experiments). Including the wind tunnel domain results in more accurate and consistent predictions from numerical simulations, with all configurations except for the detailed tyre on the open rim being within the margin of uncertainty.

5

Impact of various tyre tread patterns

Having established the need for including the wind tunnel geometry in CFD when performing direct comparisons to experiments, the flow field variations caused by the different tyre patterns are investigated. Hence, this chapter presents only uncorrected experimental data and numerical simulations including the wind tunnel. The lift forces from the simulations will be shown both with and without the correction for the parasitic WDU force, as described in Section 3.3.5. These are labelled CFD WDU and CFD, respectively.

Initially, the general trends for the force coefficients with the various tyres will be presented and compared. Next, a more detailed analysis aimed at explaining the drag variations is given. The analysis mostly focuses on the experimental results, using the CFD as a complement. These sections are followed by a presentation of the vortex structures around the wheel and how these are affected by changes to the tread pattern. Finally, the robustness and generality of the acquired results are investigated by considering a number of variations to the vehicle geometry and their effect on the tyre deltas.

5.1 Force coefficients

Figure 5.1 presents the force coefficients for the various combinations of tyres and rims. With the closed rim, a drag reduction is obtained for all patterns compared to the slick. Adding rain grooves, the drag is lowered by 0.003 C_D and with lateral grooves a reduction of 0.001 C_D is obtained. Combining the rain and lateral grooves, creating the detailed tyre, an addative reduction of 0.005 C_D is found. For the open rim, a similar decrease is obtained for the rain grooves, whereas the lateral grooves increase drag by 0.003 C_D. With the open rim a more complex combination of the effects from rain and lateral grooves is observed, with the detailed tyre being similar to the rain grooved tyre, indicating a larger interaction between the tyre and rim.

Figure 5.1 also presents the front and rear lift, C_{LF} and C_{LR}. For the tyres with rain grooves (R and D), there is a reduction in front lift for both rims. For lateral grooved tyres (L and D), there is an increase in lift, most notably at the front axle. This effect is only observed for the closed rim.

Considering the numerical predictions, the average absolute difference between the simulations and experiments is 0.002 C_D, as discussed in Section 4.1. Examining the lift forces, including the parasitic WDU lift improves the prediction significantly. The average absolute difference is

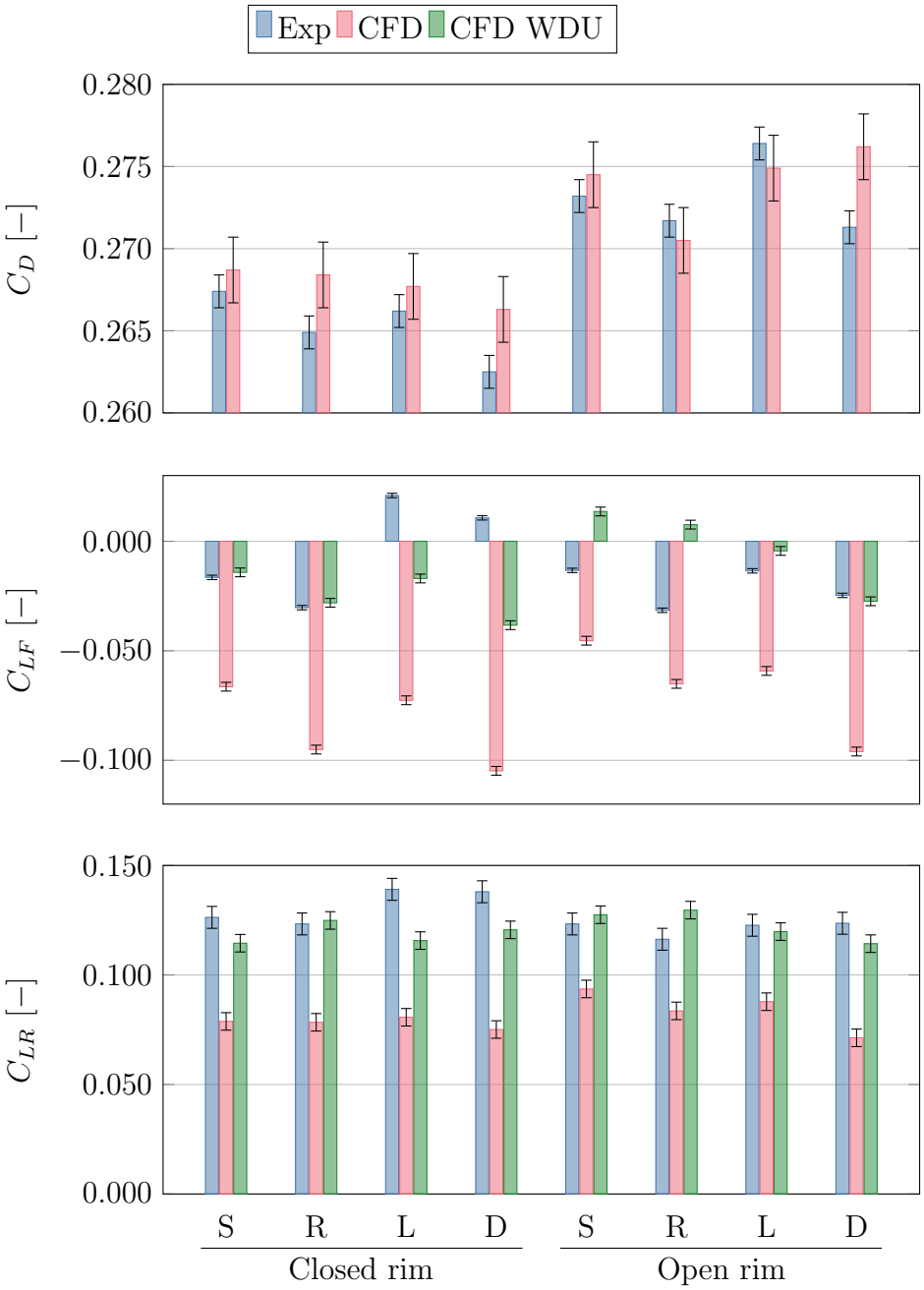

Figure 5.1: *Force coefficients from experiments and CFD. For the lift forces, CFD WDU, where the WDU lift has been included, is presented in addition to CFD.*

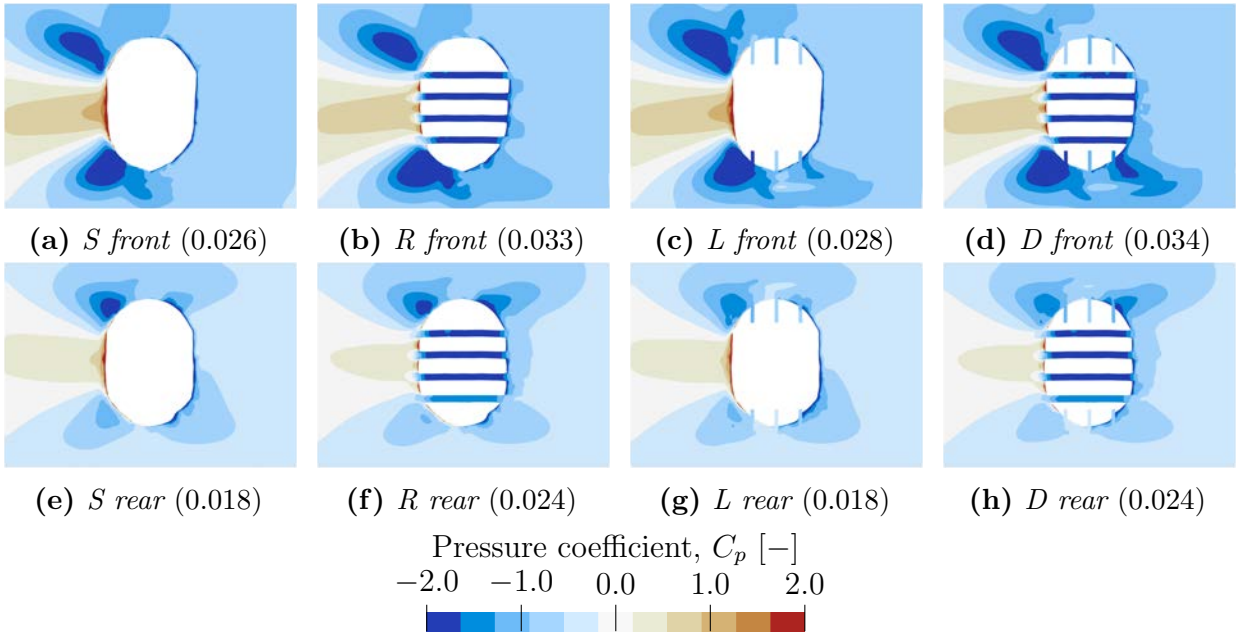

(a) *S front* (0.026) **(b)** *R front* (0.033) **(c)** *L front* (0.028) **(d)** *D front* (0.034)

(e) *S rear* (0.018) **(f)** *R rear* (0.024) **(g)** *L rear* (0.018) **(h)** *D rear* (0.024)

Figure 5.2: *Pressure coefficient from CFD at the front and rear right WDUs with the various tyres on the closed rim. The correction applied to C_{LF} or C_{LR} from the illustrated WDU is indicated in the parenthesis.*

reduced from 0.063 to 0.021 C_{LF} for the front lift and from 0.045 to 0.010 C_{LR} for the rear lift. As illustrated in Figure 5.1, the parasitic force on the WDUs varies with the tyre and is larger at the front axle. This is further explained by Figure 5.2, where the pressure on the front and rear right WDUs is shown for the different tyres with the closed rim. For tyres without rain grooves (S and L), the jetting effect, as described by Fackrell and Harvey [26], is visible with $C_p \approx 2$ right upstream the contact patch. This high-pressure region is reduced when adding rain grooves (R and D). Moreover, the acceleration through the rain grooves at the contact patch results in lower pressure, requiring higher correction factors. At the rear wheels, the acceleration at the tyre shoulder is less, resulting in smaller low-pressure regions and corrections. Investigating the pressure distribution with the open rim (not shown here) only small variations are observed, indicating that the rim design only has a limited effect on the WDU corrections.

5.2 Different tyres on the closed rim

Figure 5.3 presents the flow fields from experiments and simulations at the front wheel for the four tyres with the closed rim. For the slick tyre (Figures 5.3a and 5.3b), three dominant structures are identified; a contact patch separation, a large separation from the upper half of the wheel and a vortex from the upstream tyre shoulder. Except for a small downshift in the downstream parts of the upper structure, similar fields are obtained from both the experiment and simulation.

For the rain grooved tyre (Figures 5.3c and 5.3d), only minor differences to the slick are observed. A slight reduction in the contact patch separation is obtained and in CFD the downshift of the downstream part of the upper structure is removed. Instead, the drag reduction is found at the

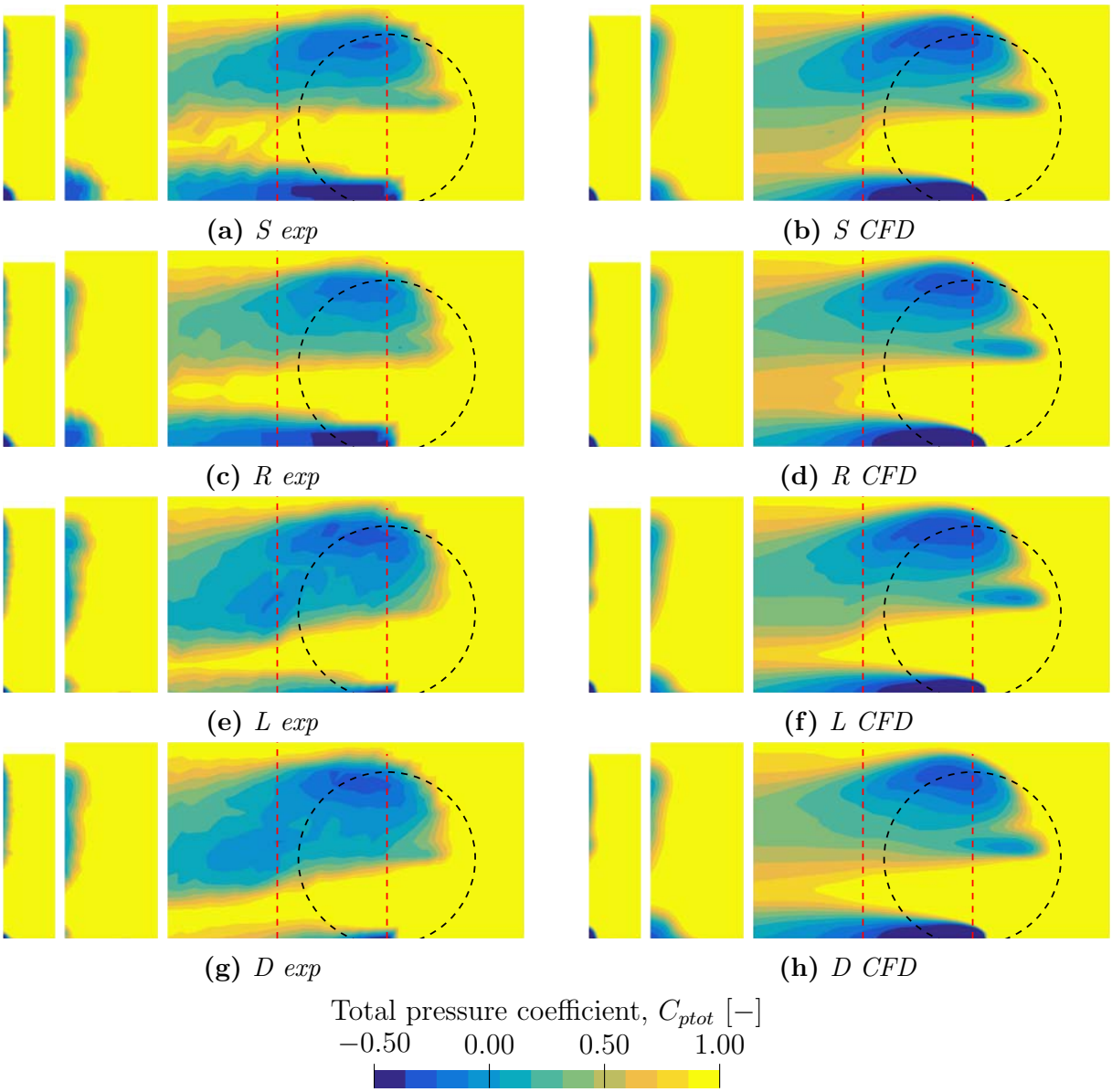

(a) *S exp* **(b)** *S CFD*

(c) *R exp* **(d)** *R CFD*

(e) *L exp* **(f)** *L CFD*

(g) *D exp* **(h)** *D CFD*

Figure 5.3: *Total pressure coefficient at the front right wheel from experiments and simulations with the closed rim. The planes are, from left to right; FW axle, FW axle* +400 mm *and FW y. In FW y, the outline of the tyre is shown along with the locations of the x-normal planes.*

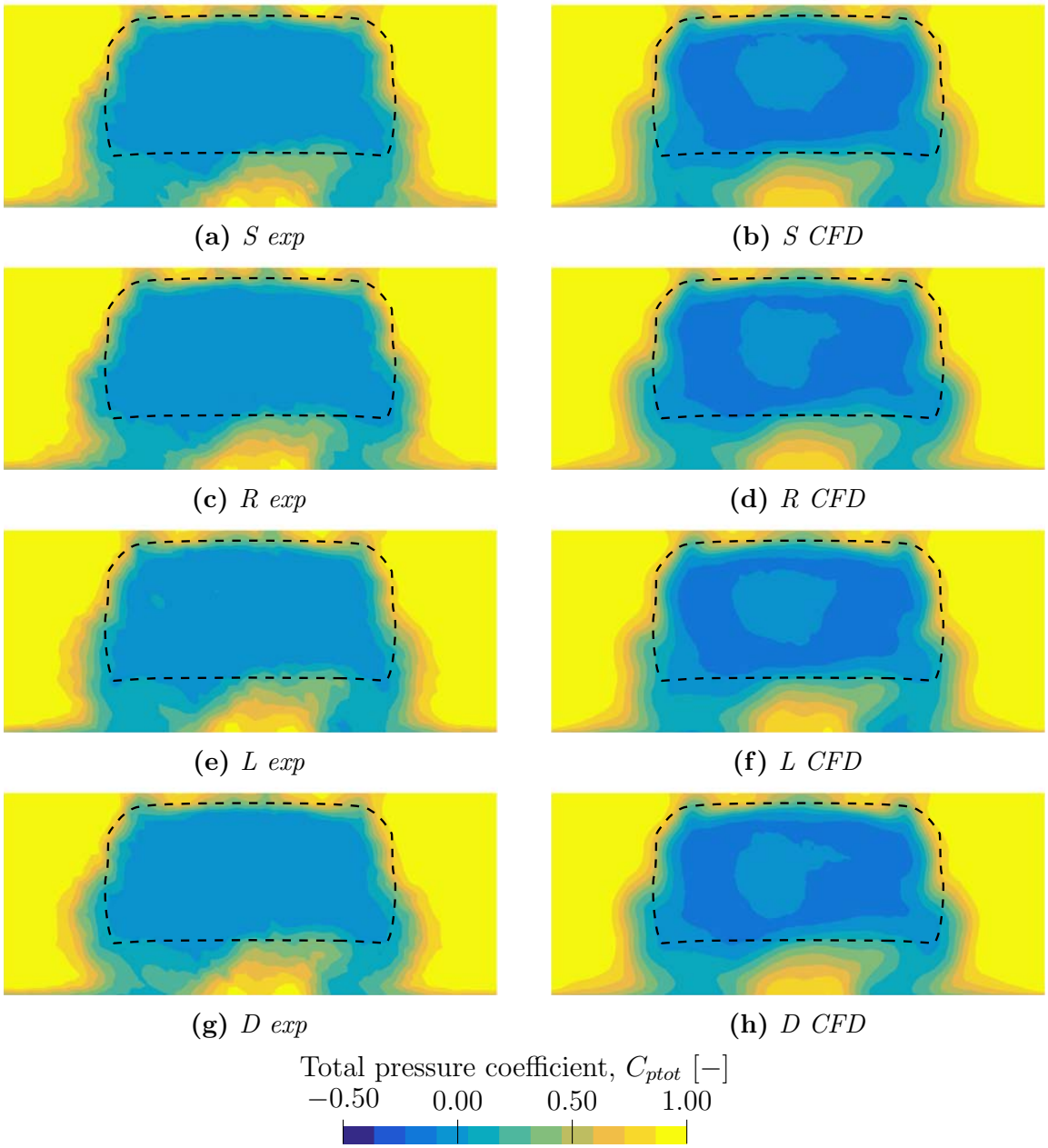

Figure 5.4: *Total pressure coefficient in the base plane from experiments and simulations with the closed rim. The dashed line marks the outline of the vehicle base.*

rear wheels, where the rain grooves increase the inflow downstream the contact patch, resulting in smaller rear wheel wakes, as observed in both experiments and simulations (Figures 5.4a to 5.4d).

When adding lateral grooves, a smaller contact patch separation is observed (Figures 5.3e and 5.3f). Comparing experiment and simulation, the reduction appears larger in the experiment. This discrepancy can be partly explained by the sampling grid employed in the experiment. A spacing of 55 mm was used in the z-direction, limiting the ability to capture sharp gradients. Furthermore, the upper separation is enlarged by the lateral grooves, extending further downwards in the rear of the plane. The changes at the front wheel are responsible for the drag reduction. This is confirmed by the base wake planes (Figures 5.4e and 5.4f) where only small differences to the slick are observed.

Combining the rain and lateral grooves to the detailed tyre a reduction of the contact patch separation is noted in the experiment, Figure 5.3g. This is only partly recreated in the simulation (Figure 5.3h), likely explaining the discrepancy in the drag prediction. The rest of the front wheel flow resembles that of the lateral grooved tyre. At the rear, the effect of the rain grooves is visible, reducing the size of the wheel wakes (Figures 5.4g and 5.4h).

Considering the lift forces, the differences between the tyres can be explained by examining the wheelhouse pressure, as described in Paper B. From the flow fields at the front wheel (Figure 5.3), a connection between increased downwash and more front lift can be identified. This link is further established by the numerical predictions of front lift. Accurate values are obtained for the slick and rain grooved tyres, which are the simulations where the trajectory of the front wheel wake is most similar to the experiments.

5.3 Different tyres on the open rim

The flow fields at the front right wheel with the open rim are shown in Figure 5.5. Comparing the flow for the open rim (Figure 5.5a) to that of the closed rim (Figure 5.3a), the largest differences are found in the lower structures, with a narrower, but taller, structure for the open rim. Examining the plane FW y in the simulation (Figure 5.5b), it is observed that the larger separation likely is a combination of the contact patch separation and a separation created by the opening of the rim. Due to the grid employed in the experiment, these cannot be separated in Figure 5.5a. Further downstream, the lower structures are larger in the experiment than in the simulation. This discrepancy is explained by the vortex moving slightly inwards in the CFD, outside the area covered by the x-normal planes. The simulation also predicts a prominent shoulder vortex, which is not distinguishable in the experiment. Finally examining the base wake, the open rim (Figures 5.6a and 5.6b) results in wider wheel wakes with larger losses than the closed rim (Figures 5.4a and 5.4b).

For the rain grooved tyre, only small changes are noted at the front wheel (Figures 5.5c and 5.5d) when compared to the slicks. Instead, similar to the closed rim, the drag reduction is found at the rear wheels where smaller wheel wakes are produced by the rain grooved tyre, Figures 5.6c and 5.6d.

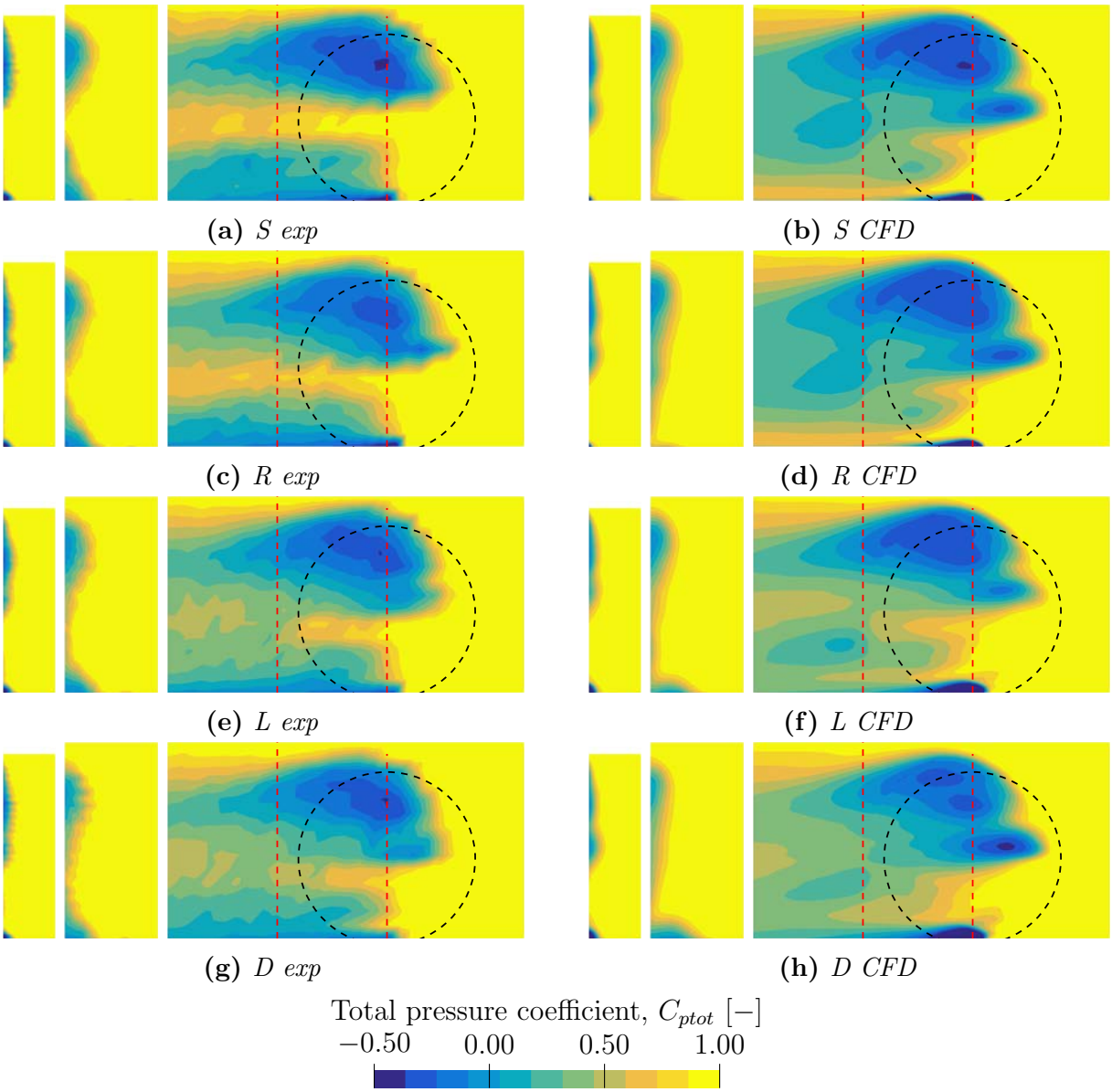

(a) *S exp* **(b)** *S CFD*

(c) *R exp* **(d)** *R CFD*

(e) *L exp* **(f)** *L CFD*

(g) *D exp* **(h)** *D CFD*

Figure 5.5: *Total pressure coefficient at the front right wheel from experiments and simulations with the open rim. The planes are, from left to right; FW axle, FW axle* +400 mm *and FW y. In FW y, the outline of the tyre is shown along with the locations of the x-normal planes.*

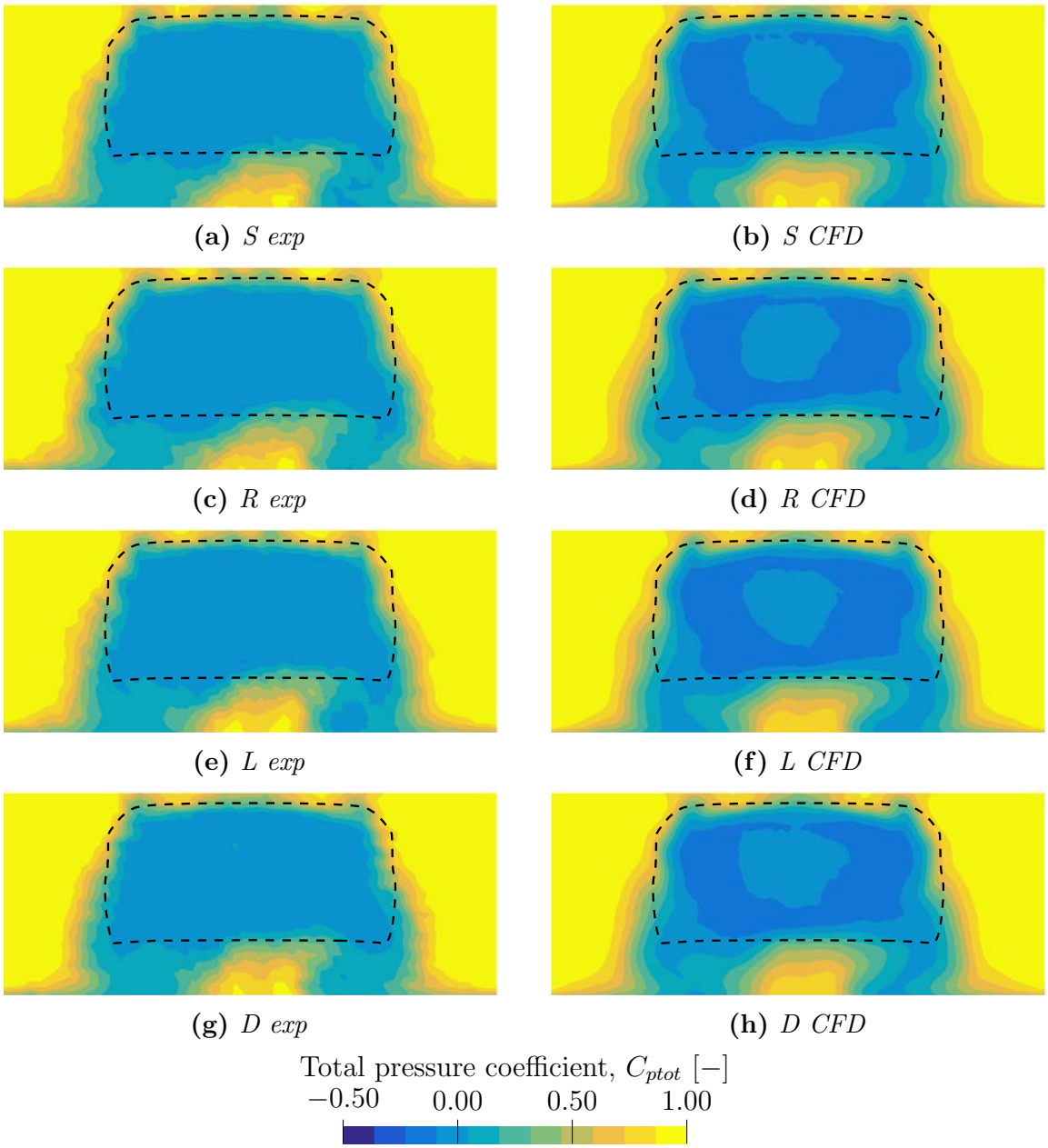

Figure 5.6: *Total pressure coefficient in the base plane from experiments and simulations with the open rim. The dashed line marks the outline of the vehicle base.*

Table 5.1: *The changes of the vortices in Figures 5.7 and 5.8 when varying the rim and tread pattern. The arrows indicate whether a vortex increases or decreases, as indicated by the vorticity magnitude and vortex size. No significant change is indicated by -.*

Vortex	Closed to open rim	Add rain grooves	Add lateral grooves
A	↑	↓	↓
B	↓	↓	↓
C inner	-	↓	↓
C outer	Appears	↑	↑
D	↑	↑	More downwash
E lower	↑	↑	↑
E upper	↑	↓	-
F	-	-	-
G	Appears	-	↓

With the lateral grooved tyre, the drag increase mainly occurs at the front wheels where the upper separation is enlarged, extending further down (Figures 5.5e and 5.5f). Further analysis of the numerical simulation indicates that the increase is caused by the interaction between the lateral grooves and the rim. At the tyre shoulder, the lateral grooves trigger a separation. For the closed rim, the flow soon reattaches, resulting in an overall small effect. For the open rim, the separation instead grows due to the interaction with the flow through the rim, leading to additional drag.

From the flow fields at the front wheel (Figures 5.5g and 5.5h) it is observed that the detailed tyre results in a larger upper separation and a slightly smaller lower structure. Instead, the drag reduction is mainly found at the rear wheels where a flow field similar to that of the rain grooved tyre is obtained, Figures 5.6g and 5.6h. Given that the overall drag is similar to the rain grooved tyre, despite the suspected drag penalty from the lateral grooves at the front wheels, the drag-reducing mechanism at the rear wheels is stronger for the detailed than for the rain grooved tyre, indicating synergy between the alterations at the front and rear wheels.

5.4 Vortex structures

The flow mechanisms can be further understood by investigating the vortex structures at the front wheel. Using the slick tyre with both the closed and open rims as the baselines, the main structures are identified, Figure 5.7. Combining this knowledge with the flow field measurements (Figures 5.3 and 5.5), a schematic sketch, similar to that of Wäschle [9], is constructed, Figure 5.8.

The impact of varying the tyre and rim on the identified vortices is summarised in Table 5.1. Additionally to the vortices presented in Table 5.1, Figure 5.7b illustrates a vortex labelled α. This vortex rotates clockwise and originates from the velocity difference between the stationary floor and the WDU. Similar structures were found also at the other WDU edges. The presence of these vortices reinforces the need for including the wind tunnel geometry in simulations when performing direct comparisons between experiments and CFD.

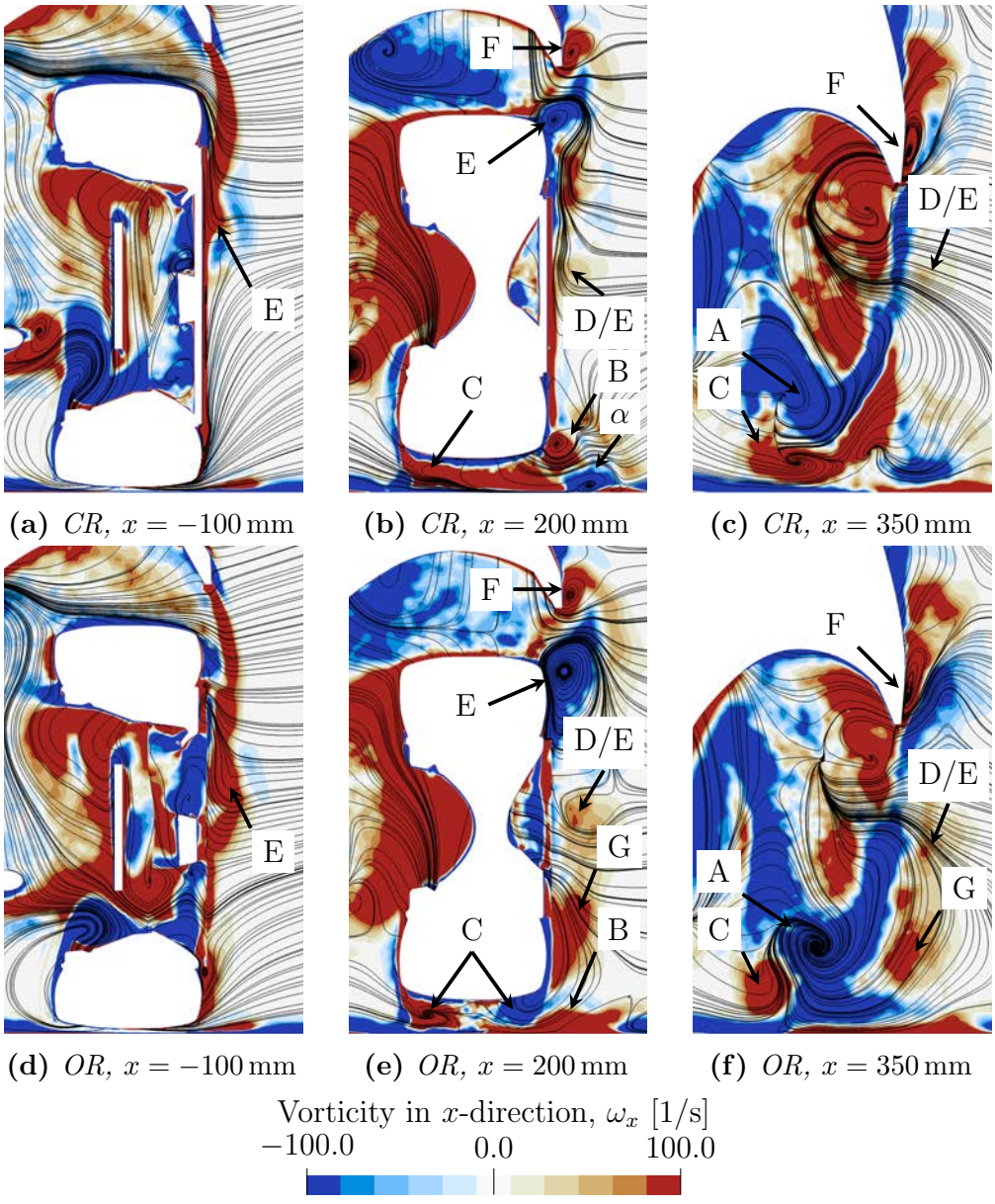

(a) *CR*, $x = -100\,\text{mm}$ **(b)** *CR*, $x = 200\,\text{mm}$ **(c)** *CR*, $x = 350\,\text{mm}$

(d) *OR*, $x = -100\,\text{mm}$ **(e)** *OR*, $x = 200\,\text{mm}$ **(f)** *OR*, $x = 350\,\text{mm}$

Figure 5.7: *Streamlines and x-component of vorticity from CFD at the front right wheel observed from behind. The results are presented for the slick tyre with both closed and open rims.*

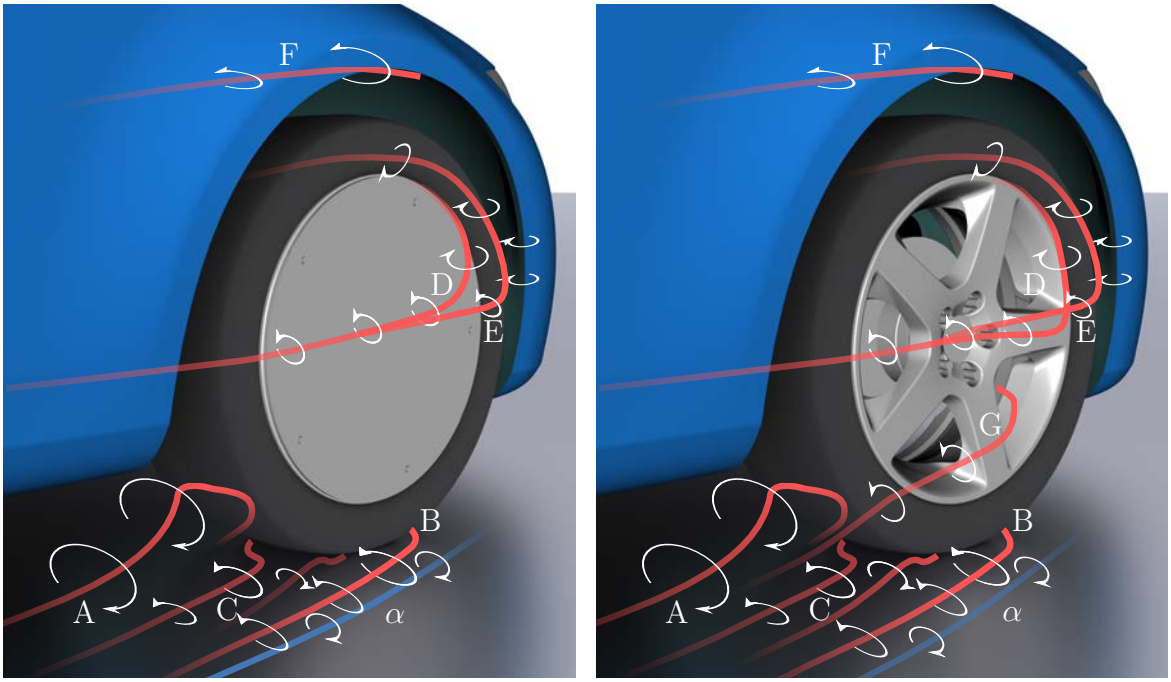

(a) *Closed rim* **(b)** *Open rim*

Figure 5.8: *Schematic sketch of the vortex structures at the front right wheel seen from behind. Inspired by [9].*

5.5 Effect of vehicle geometry

Previous research has shown that the influence from varying the tyre can be vehicle dependent, as demonstrated by for example [8, 15, 45]. The extensive set of experimental data collected during the test campaign can be used to understand the sensitivity and generality of the effects discussed throughout this chapter.

Until this point, a single vehicle configuration has been considered, the DrivAer notchback with closed cooling, hereafter called the baseline. Apart from the baseline, the tyres were also tested with a front wheel deflector (FWD) fitted, with open cooling (OC) and with the combination of the two (FWD & OC). This was performed for both closed and open rims. For the closed rim, the same configurations were also evaluated with the DrivAer squareback. The configurations are shown in Figure 5.9.

Figure 5.10 shows how the drag changes between the slick and patterned tyres for the various configurations. Adding rain grooves (Figure 5.10a), the drag is reduced for all cases, with the largest differences observed for the squareback. The sensitivity is larger for the lateral grooved tyre (Figure 5.10b), both to the rim and the front wheel deflector. The latter suggests that the impact of lateral grooves likely is vehicle dependent, which is reinforced by the results of Hobeika and Sebben [45] who tested the same wheels on a Volvo S60 and found that lateral grooves increased drag. With the detailed tyre (Figure 5.10c), the dependency on the rim and front wheel deflector remains but are slightly smaller than for the lateral grooved tyre.

Comparing the delta between slick and detailed tyres to those presented by both Hobeika and

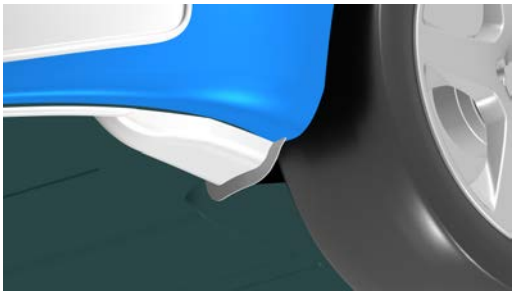

(a) *Front wheel deflector (FWD)*

(b) *Open cooling (OC)*

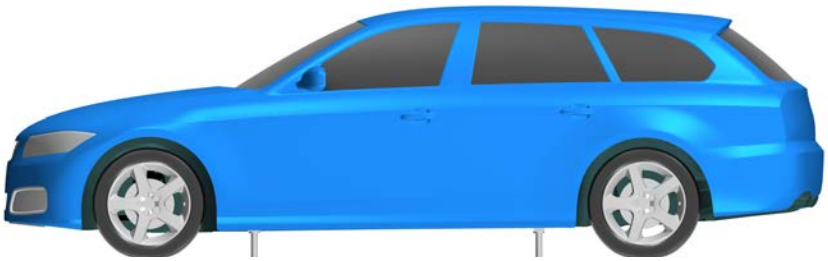

(c) *Squareback*

Figure 5.9: *Configurations investigated when considering the sensitivity of the tyre configurations.*

Sebben [52] and Wickern et al. [8], there is a good agreement for the closed rim, with a drag reduction of approximately 0.005 C_D obtained in all works. However, for the open rim, both Hobeika and Sebben [45] and Wickern et al. [8] report a small drag increase of 0.001-0.002 C_D, whereas this work finds a reduction of 0.002 C_D, suggesting that the vehicle dependency is stronger with the open rim.

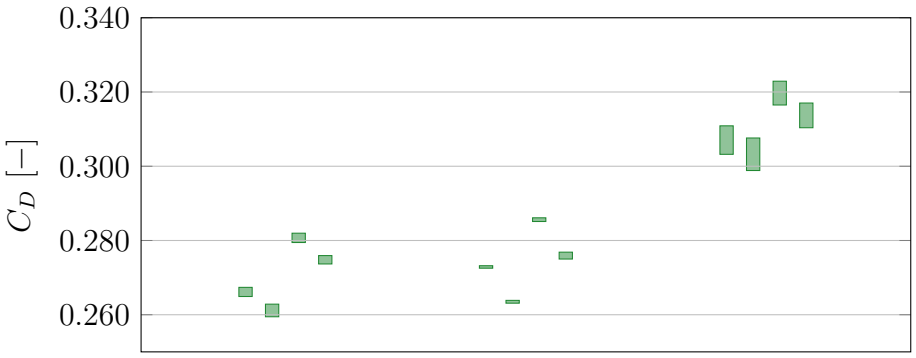

(a) *Slick to rain grooved*

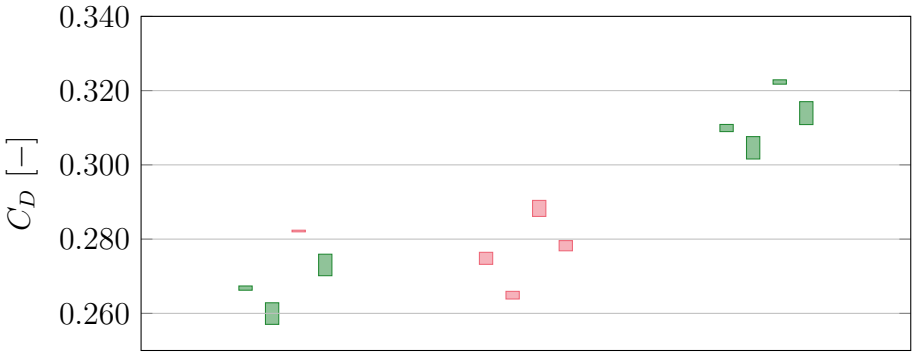

(b) *Slick to lateral grooved*

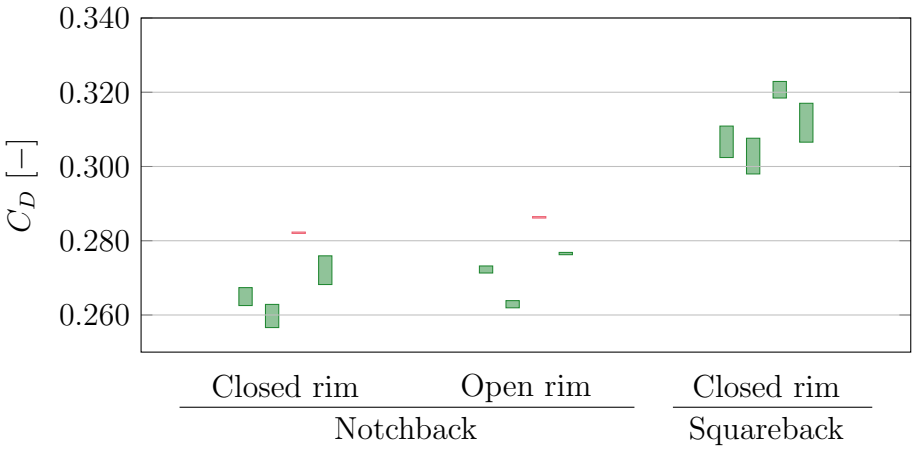

(c) *Slick to detailed*

Figure 5.10: *Change in drag between the slick and the various tyres for different configurations. A green bar indicates that the drag is lower for the patterned tyre. The configurations within each group are, from left to right; baseline, FWD, OC, FWD & OC. Data from experiments.*

6

Concluding remarks

The objectives of this thesis have been to investigate wheel flows for a passenger vehicle. Firstly, the impact of the wind tunnel was assessed by comparing experiments to CFD with and without the wind tunnel geometry. Secondly, the influence of varying the tyre pattern was analysed using measurements from the wind tunnel and numerical simulations. As part of the two studies, a numerical method for studying wheel flows was established, implemented and correlated towards experimental data.

The study of wind tunnel interference combined experiments and numerical simulations to determine how the wind tunnel affects the flow around wheels. Simulations where the geometry of the wind tunnel was included, in contrast to replicating open road conditions, were compared to uncorrected and blockage corrected experimental results. Including the wind tunnel in CFD improved the drag prediction. The largest differences between open road and wind tunnel simulations were found when comparing tyres with and without lateral grooves, as well as between open and closed rims for the slick and rain grooved tyres. For these cases, including the wind tunnel altered the separations at the tyre shoulder or outer rim surface. The two main differences between the wind tunnel and open road are the blockage and ground simulation. It was shown that both have a non-negligible impact on the flow field.

Investigating the effect of varying the tyre tread pattern, a consistent drag reduction was found when adding rain grooves, whereas the influence of adding lateral grooves was more dependent on the rim. For the rain grooves, the main drag-reducing mechanism was found at the rear wheels, where a stronger inflow reduced the size of the wheel wakes. In the case of the lateral grooves, the most significant changes were found at the front wheel, both at the contact patch and in the interaction between the tyre and the rim. For the lift, the differences between the tyres were explained by variations in wheelhouse pressure. Examining the flow field measurements and the front lift, a connection between increased downwash and additional front lift was identified. Moreover, simulations that replicated the amount of downwash were found to result in a more accurate prediction of front lift. The importance of considering the parasitic lift force on the WDUs was demonstrated.

6.1 Future work

The importance of considering wind tunnel interference effects has been established and a numerical method for simulating wheel flows has been developed and validated to experimental data. These are essential tools and knowledge for future work aimed at increasing the

understanding of wheel aerodynamics.

Future work is targeted at examining other tyre features and determining their aerodynamic influence. Such features include varying the tyre profile, investigating more realistic tyre patterns and examining the effect of different tyre details. Using tyres designed for road usage, a method for replicating the dynamic deformations, caused by the rotational forces, is needed. Such a method could utilise either CAE methods, such as finite element analysis, physical measurements, or a combination of the two.

Moreover, the correction for the parasitic forces acting on the WDUs will be further investigated. Gathering additional experimental data of the flow field around the WDUs, combined with more numerical simulations, the aim is to better understand how a suitable correction can be determined and which factors influence the correction.

Finally, other vehicle geometries, including production vehicles, will be considered.

7

Summary of papers

7.1 Paper A

Evaluation of Wind Tunnel Interference on Numerical Prediction of Wheel Aerodynamics

The objective of this paper is to determine the influence of the wind tunnel on the flow around wheels. Wind tunnel tests were performed using a full-scale DrivAer model. In the paper, the experiments are compared to two types of numerical simulations, denoted open road and PVT. In the former, a large domain with negligible blockage and a fully moving ground was used, whereas, in the PVT setup, the geometry and ground simulation system of the wind tunnel was replicated. The results from open road and PVT are compared to blockage corrected and uncorrected experimental results, respectively. It is shown that the prediction of drag improves when including the wind tunnel geometry, both in terms of absolute values and deltas between the various tyre and rim configurations. The paper demonstrates how the differences in both blockage and ground simulation between the domains affect the flow.

7.2 Paper B

Investigation of Tyre Pattern Effect on the Aerodynamics of a Passenger Vehicle

Using the data of Paper A, this paper presents how different tyre tread patterns alter the flow. Experimental force measurements, surface pressures and flow fields are presented. For deeper analysis, the numerical simulations with the PVT setup are included. It is found that the drag is consistently reduced by adding rain grooves to a slick tyre, whereas for lateral grooves, the change is more dependent on the rim design. Moreover, it is shown how the patterns alter the lift forces and how the lift variations connect to changes in the flow field. When presenting the lift forces, the importance of including the lift on the WDUs is illustrated. Finally, the vortex structures at the front wheel, and how they vary with the tread pattern, is analysed.

References

[1] Josefsson, E., Hobeika, T., and Sebben, S. "Evaluation of Wind Tunnel Interference on Numerical Prediction of Wheel Aerodynamics". *Accepted for publication in Journal of Wind Engineering and Industrial Aerodynamics* (2022).

[2] Josefsson, E. et al. "Investigation of Tyre Pattern Effect on the Aerodynamics of a Passenger Vehicle". *Submitted to Journal of Fluids Engineering* (2022).

[3] European Environment Agency. "National Emissions Reported to the UNFCCC and to the EU Greenhouse Gas Monitoring Mechanism". Data. 2021-12. URL: https://www.eea.europa.eu/data-and-maps/data/national-emissions-reported-to-the-unfccc-and-to-the-eu-greenhouse-gas-monitoring-mechanism-17 (visited on 2021-12-15).

[4] Yang, Z. and Bandivadekar, A. "2017 Global Update: Light-duty Vehicle Greenhouse Gas and Fuel Economy Standards". 2017. URL: https://theicct.org/publications/2017-global-update-LDV-GHG-FE-standards (visited on 2020-12-01).

[5] "United Nations Global Technical Regulation on Worldwide Harmonized Light Vehicles Test Procedures (WLTP)". United Nations GTR/ECE/TRANS/180/Add.15/Amend.4, 2018-09.

[6] Schuetz, T. C. "Aerodynamics of Road Vehicles, Fifth Edition". Warrendale, PA: SAE International, 2015-12. ISBN: 978-0-7680-8253-1. DOI: 10.4271/r-430.

[7] Cogotti, A. "Aerodynamic Characteristics of Car Wheels". *Int. J. of Vehicle Design* (1983).

[8] Wickern, G., Zwicker, K., and Pfadenhauer, M. "Rotating Wheels - Their Impact on Wind Tunnel Test Techniques and on Vehicle Drag Results". *SAE transactions* (1997-02), 254–270. DOI: 10.4271/970133.

[9] Wäschle, A. "The Influence of Rotating Wheels on Vehicle Aerodynamics - Numerical and Experimental Investigations". *SAE Technical Paper 2007-01-0107* (2007-04). DOI: 10.4271/2007-01-0107.

[10] Wang, Y. et al. "Experimental Study of Wheel-Vehicle Aerodynamic Interactions". *Journal of Wind Engineering and Industrial Aerodynamics* **198** (2020-03). ISSN: 01676105. DOI: 10.1016/j.jweia.2019.104062.

[11] Elofsson, P. and Bannister, M. "Drag Reduction Mechanisms Due to Moving Ground and Wheel Rotation in Passenger Cars". *SAE 2002 World Congress & Exhibition*. 2002-03. DOI: 10.4271/2002-01-0531.

[12] Fu, C., Uddin, M., and Zhang, C. "Computational Analyses of the Effects of Wind Tunnel Ground Simulation and Blockage Ratio on the Aerodynamic Prediction of Flow over a Passenger Vehicle". *Vehicles* **2**.2 (2020-06), 318–341. ISSN: 2624-8921. DOI: 10.3390/vehicles2020018.

[13] Jakirlic, S. et al. "Eddy-Resolving Simulations of the Notchback 'DrivAer' Model: Influence of Underbody Geometry and Wheels Rotation on Aerodynamic Behaviour". *SAE Technical Paper 2016-01-1602* (2016-04). DOI: 10.4271/2016-01-1602.

[14] Landström, C., Löfdahl, L., and Walker, T. "Detailed Flow Studies in Close Proximity of Rotating Wheels on a Passenger Car". *SAE International Journal of Passenger Cars - Mechanical Systems* **2**.1 (2009-04), 861–874. ISSN: 1946-4002. DOI: 10.4271/2009-01-0778.

[15] Mercker, E. et al. "On the Aerodynamic Interference Due to the Rolling Wheels of Passenger Cars". *SAE Transactions* **100** (1991), 460–476. ISSN: 0096-736X.

[16] Aultman, M. et al. "Effects of Wheel Rotation on Long-Period Wake Dynamics of the DrivAer Fastback Model". *Fluids* **7**.1 (2022-01). ISSN: 2311-5521. DOI: 10.3390/fluids7010019.

[17] Schnepf, B., Tesch, G., and Indinger, T. "On the Influence of Ride Height Changes on the Aerodynamic Performance of Wheel Designs". *International Journal of Automotive Engineering* **6**.1 (2015), 23–29. ISSN: 2185-0984, 2185-0992. DOI: 10.20485/jsaeijae.6.1_23.

[18] Brandt, A. et al. "The Effects of Wheel Design on the Aerodynamic Drag of Passenger Vehicles". *SAE Int. J. Adv. & Curr. Prac. in Mobility* **1**.3 (2019-04), 1279–1299. ISSN: 2641-9637. DOI: 10.4271/2019-01-0662.

[19] D'Hooge, A. et al. "The Aerodynamic Development of the Tesla Model S - Part 2: Wheel Design Optimization". *SAE 2012 World Congress & Exhibition*. 2012-04. DOI: 10.4271/2012-01-0178.

[20] Hirose, K., Kawamata, H., and Oshima, M. "Aerodynamic Sensitivity Analysis of Wheel Shape Factors". *SAE Int. J. Adv. & Curr. Prac. in Mobility* **1**.3 (2019-04), 1300–1310. DOI: 10.4271/2019-01-0667.

[21] Haag, L. et al. "Numerical and Experimental Investigations of Rotating Wheel Aerodynamics on the DrivAer Model With Engine Bay Flow". *ASME 2017 Fluids Engineering Division Summer Meeting*. 2017-07. DOI: 10.1115/FEDSM2017-69305.

[22] Koitrand, S., Gaylard, A., and Fiet, G. O. "An Investigation of Wheel Aerodynamic Effects for a Saloon Car". *Proceedings of the 10th FKFS-Conference*. 2015, pp. 240–255.

[23] Vdovin, A. et al. "Investigation of Wheel Ventilation-Drag Using a Modular Wheel Design Concept". *SAE International Journal of Passenger Cars - Mechanical Systems* **6**.1 (2013-04), 308–315. ISSN: 1946-4002. DOI: 10.4271/2013-01-0953.

[24] Vdovin, A., Löfdahl, L., and Sebben, S. "Investigation of Wheel Aerodynamic Resistance of Passenger Cars". *SAE International Journal of Passenger Cars - Mechanical Systems* **7**.2 (2014-04), 639–645. ISSN: 1946-4002. DOI: 10.4271/2014-01-0606.

[25] Mayer, W. and Wiedemann, J. "The Influence of Rotating Wheels on Total Road Load". *SAE Technical Paper 2007-01-1047* (2007-04). ISSN: 0148-7191. DOI: 10.4271/2007-01-1047.

[26] Fackrell, J. E. and Harvey, J. K. "The Flow Field and Pressure Distribution of an Isolated Road Wheel". *Advances in Road Vehicle Aerodynamics*. Vol. 10. 1973, pp. 155–165.

[27] Mears, A. P., Dominy, R. G., and Sims-Williams, D. B. "The Air Flow About an Exposed Racing Wheel". *Motorsports Engineering Conference & Exhibition*. 2002-12. DOI: 10.4271/2002-01-3290.

[28] Croner, E. et al. "Aerodynamic Characterization of the Wake of an Isolated Rolling Wheel". *International Journal of Heat and Fluid Flow* **43** (2013-10), 233–243. ISSN: 0142727X. DOI: 10.1016/j.ijheatfluidflow.2013.04.008.

[29] Axerio-Cilies, J. et al. "An Aerodynamic Investigation of an Isolated Stationary Formula 1 Wheel Assembly". *Journal of fluids engineering* **134**.2 (2012). ISSN: 0098-2202. DOI: 10.1115/1.4005768.

[30] Axon, L., Garry, K., and Howell, J. "An Evaluation of CFD for Modelling the Flow around Stationary and Rotating Isolated Wheels". *SAE transactions* **107** (1998), 205–215. ISSN: 0096-736X. DOI: 10.4271/980032.

[31] Diasinos, S., Barber, T. J., and Doig, G. "The Effects of Simplifications on Isolated Wheel Aerodynamics". *Journal of Wind Engineering and Industrial Aerodynamics* **146** (2015-11), 90–101. ISSN: 01676105. DOI: 10.1016/j.jweia.2015.08.004.

[32] Lew, C. et al. "Aerodynamic Simulation of a Standalone Rotating Treaded Tire". *SAE Technical Paper 2017-01-1551* (2017-03). DOI: 10.4271/2017-01-1551.

[33] Mortazawy, M. et al. "Aerodynamic Simulation of a Standalone Round and Deforming Treaded Tire". *SAE Int. J. Advances & Curr. Prac. in Mobility* **3**.5 (2021-04), 2227–2235. ISSN: 2641-9637. DOI: 10.4271/2021-01-0948.

[34] Mears, A. P. and Dominy, R. G. "Racing Car Wheel Aerodynamics – Comparisons between Experimental and CFD Derived Flow-Field Data". *Motorsports Engineering Conference & Exposition*. 2004-11. DOI: 10.4271/2004-01-3555.

[35] Pirozzoli, S., Orlandi, P., and Bernardini, M. "The Fluid Dynamics of Rolling Wheels at Low Reynolds Number". *Journal of Fluid Mechanics* **706** (2012-09), 496–533. ISSN: 0022-1120, 1469-7645. DOI: 10.1017/jfm.2012.273.

[36] Reiß, J., Haag, L., and Indinger, T. "CFD Investigation on Fully Detailed and Deformed Car Tires". *International Journal of Automotive Engineering* **10**.4 (2019), 324–331. ISSN: 2185-0984. DOI: 10.20485/jsaeijae.10.4_324.

[37] Reiß, J. et al. "Experimental and Numerical Investigations on Isolated, Treaded and Rotating Car Wheels". *SAE Technical Paper 2020-01-0686* (2020-04). ISSN: 0148-7191. DOI: 10.4271/2020-01-0686.

[38] Schnepf, B., Tesch, G., and Indinger, T. "Investigations on the Flow Around Wheels Using Different Road Simulation Tools". *Proceedings of the 9th FKFS-Conference*. Stuttgart, 2013.

[39] Schnepf, B., Schütz, T., and Indinger, T. "Further Investigations on the Flow Around a Rotating, Isolated Wheel with Detailed Tread Pattern". *SAE International Journal of Passenger Cars - Mechanical Systems* **8**.1 (2015-04), 261–274. ISSN: 1946-4002. DOI: 10.4271/2015-01-1554.

[40] Sprot, A. J., Sims-Williams, D. B., and Dominy, R. G. "The Aerodynamic Characteristics of a Fully Deformable Formula One Wind Tunnel Tyre". *SAE International Journal of Passenger Cars - Mechanical Systems* **5**.2 (2012-04), 1026–1041. ISSN: 1946-4002. DOI: 10.4271/2012-01-1166.

[41] Vilar Cánovas, J. and Antoniadis, A. F. "Computational Modelling of a Solid and Deformed Automotive Rotating Wheel in Contact with the Ground". *Proceedings of the Institution of Mechanical Engineers, Part D: Journal of Automobile Engineering* **234**.5 (2020-04), 1413–1424. ISSN: 0954-4070, 2041-2991. DOI: 10.1177/0954407019877302.

[42] Axon, L., Garry, K., and Howell, J. "The Influence of Ground Condition on the Flow Around a Wheel Located Within a Wheelhouse Cavity". *International Congress & Exposition*. 1999-03. DOI: 10.4271/1999-01-0806.

[43] Kulak, M. et al. "Numerical and Experimental Analysis of Rotating Wheel in Contact with the Ground". *International Journal of Numerical Methods for Heat & Fluid Flow* (2018-05). ISSN: 0961-5539. DOI: 10.1108/HFF-06-2017-0257.

[44] Wittmeier, F. et al. "Model Scale Based Process for the Development of Aerodynamic Tire Characteristics". *SAE Technical Paper 2014-01-0585* (2014-04). DOI: 10.4271/2014-01-0585.

[45] Hobeika, T. and Sebben, S. "Tyre Pattern Features and Their Effects on Passenger Vehicle Drag". *SAE International Journal of Passenger Cars - Mechanical Systems* **11**.5 (2018-04), 401–413. ISSN: 1946-4002. DOI: 10.4271/2018-01-0710.

[46] Mlinaric, P. "Investigation of the Influence of Tyre Deformation and Tyre Contact Patch on CFD Predictions of Aerodynamic Forces on a Passenger Car". MA thesis. Gothenburg: Chalmers University of Technology, 2007.

[47] Landström, C. et al. "Aerodynamic Effects of Different Tire Models on a Sedan Type Passenger Car". *SAE International Journal of Passenger Cars - Mechanical Systems* **5**.1 (2012-04), 136–151. ISSN: 1946-4002. DOI: 10.4271/2012-01-0169.

[48] Ogawa, A. et al. "Development Methodologies for Formula One Aerodynamics". *Honda R&D Technical Review* (2009).

[49] Gray, M. et al. "Improved Methodology for Realistic Representation of Rotating Wheels in CFD Applications". *Progress in Vehicle Aerodynamics and Thermal Management*. Stuttgart, 2019.

[50] Croner, E. "Etude de l'écoulement autour des ensembles roulants d'un véhicule en vue de l'optimisation aérodynamique du pneumatique". PhD thesis. Université de Toulouse, 2014.

[51] Vdovin, A. et al. "Investigation of Vehicle Ride Height and Wheel Position Influence on the Aerodynamic Forces of Ground Vehicles". *The International Vehicle Aerodynamics Conference*. Loughborough: Woodhead Publishing, 2014-10, pp. 81–90. ISBN: 978-0-08-100199-8. DOI: 10.1533/9780081002452.3.81.

[52] Hobeika, T. and Sebben, S. "CFD Investigation on Wheel Rotation Modelling". *Journal of Wind Engineering and Industrial Aerodynamics* **174** (2018-03), 241–251. ISSN: 01676105. DOI: 10.1016/j.jweia.2018.01.005.

[53] Alexias, P., Hobeika, T., and Villiers, E. D. "An Automated Method for the Aerodynamic Modelling of Grooved Tires". *2019 JSAE Annual Congress (Autumn)*. JSAE, 2019-05.

[54] Truck and Bus Aerodynamics and Fuel Economy Committee. "Guidelines for Aerodynamic Assessment of Medium and Heavy Commercial Ground Vehicles Using Computational Fluid Dynamics". Tech. rep. SAE International, 2021-06. DOI: 10.4271/J2966_202106.

[55] Katz, J. "Race Car Aerodynamics: Designing for Speed". R. Bentley, 1995. ISBN: 0-8376-0142-8.

[56] Collin, C., Indinger, T., and Müller, J. "Moving Ground Simulation for High Performance Race Cars in an Automotive Wind Tunnel-CFD Approach on Moving Belt Dimensions". *International Journal of Automotive Engineering* **8**.1 (2017), 15–21. ISSN: 2185-0984. DOI: 10.20485/jsaeijae.8.1_15.

[57] Fischer, O. et al. "CFD Validation Study for a Sedan Scale Model in an Open Jet Wind Tunnel". *SAE Technical Paper 2008-01-0325* (2008-04). ISSN: 0148-7191. DOI: 10.4271/2008-01-0325.

[58] Fischer, O. et al. "CFD Approach to Evaluate Wind-Tunnel and Model Setup Effects on Aerodynamic Drag and Lift for Detailed Vehicles". *SAE Technical Paper 2010-01-0760* (2010-04). ISSN: 0148-7191. DOI: 10.4271/2010-01-0760.

[59] Cyr, S., Ih, K.-D., and Park, S.-H. "Accurate Reproduction of Wind-Tunnel Results with CFD". *SAE Technical Paper 2011-01-0158* (2011-04). ISSN: 0148-7191. DOI: 10.4271/2011-01-0158.

[60] Ljungskog, E., Sebben, S., and Broniewicz, A. "Inclusion of the Physical Wind Tunnel in Vehicle CFD Simulations for Improved Prediction Quality". *Journal of Wind Engineering and Industrial Aerodynamics* **197** (2019-12). ISSN: 0167-6105. DOI: 10.1016/j.jweia.2019.104055.

[61] Wickern, G. and Beese, E. "Computational and Experimental Evaluation of a Pad Correction for a Wind Tunnel Balance Equipped for Rotating Wheels". *SAE Technical Paper 2002-01-0532* (2002-03). ISSN: 0148-7191. DOI: 10.4271/2002-01-0532.

[62] Blumrich, R. et al. "New FKFS Technology at the Full-Scale Aeroacoustic Wind Tunnel of University of Stuttgart". *SAE International Journal of Passenger Cars - Mechanical Systems* **8**.1 (2015-04), 294–305. ISSN: 1946-4002. DOI: 10.4271/2015-01-1557.

[63] Heft, A. I., Indinger, T., and Adams, N. A. "Introduction of a New Realistic Generic Car Model for Aerodynamic Investigations". *SAE Technical Paper 2012-01-0168* (2012). ISSN: 0148-7191. DOI: 10.4271/2012-01-0168.

[64] Hupertz, B. et al. "Introduction of a New Full-Scale Open Cooling Version of the DrivAer Generic Car Model". *Progress in Vehicle Aerodynamics and Thermal Management*. Cham: Springer International Publishing, 2018, pp. 35–60. DOI: 10.1007/978-3-319-67822-1_3.

[65] Hupertz, B. et al. "On the Aerodynamics of the Notchback Open Cooling DrivAer: A Detailed Investigation of Wind Tunnel Data for Improved Correlation and Reference". *SAE Technical Paper 2021-01-0958* (2021-04). DOI: 10.4271/2021-01-0958.

[66] Ashton, N. et al. "First Automotive CFD Prediction Workshop, Cross-Plotting - Case2a/b". Oxford, 2019. URL: https://autocfd1.s3.eu-west-1.amazonaws.com/Presentations/Case2-summary-v2.pdf (visited on 2021-08-21).

[67] Sternéus, J., Walker, T., and Bender, T. "Upgrade of the Volvo Cars Aerodynamic Wind Tunnel". *SAE Technical Paper 2007-01-1043* (2007-04). DOI: 10.4271/2007-01-1043.

[68] Aeroprobe corporation. "Standard Probes User Manual". 2015.

[69] Sterken, L. et al. "Experimental and Numerical Investigations of the Base Wake on an SUV". *SAE Technical Paper Series* **1** (2013). DOI: 10.4271/2013-01-0464.

[70] Eng, M. and Walker, T. "Investigation of Aerodynamic Correction Methods Applied to a Slotted Wall Wind Tunnel". *Proceedings of Euromech Colloquium 509*. Berlin, 2009-03, pp. 59–69. URL: https://depositonce.tu-berlin.de/handle/11303/2466.

[71] Davidson, L. "Large Eddy Simulations: How to Evaluate Resolution". *International Journal of Heat and Fluid Flow* **30**.5 (2009), 1016–1025. DOI: 10.1016/j.ijheatfluidflow.2009.06.006.

[72] Ekman, P. et al. "Accuracy and Speed for Scale-Resolving Simulations of the DrivAer Reference Model". *SAE Technical Paper 2019-01-0639* (2019-04). DOI: 10.4271/2019-01-0639.